Modeling Near-Inertial Waves in Lake Superior

A THESIS
SUBMITTED TO THE FACULTY OF THE GRADUATE SCHOOL
OF THE UNIVERSITY OF MINNESOTA
BY

Lucas J Gloege

IN PARTIAL FULFILLMENT OF THE REQUIREMENTS
FOR THE DEGREE OF
MASTER OF SCIENCE

Advisor : Jay Austin

July, 2014

Acknowledgements

Many people have contributed to my success in completing this thesis. First and foremost, I need to thank my advisor Dr. Jay Austin, from whom I have learned a great deal about scientific research. His patience, guidance, and suggestions greatly improved the the quality of this thesis. I thank my committee members, Dr. Sam Kelley and Dr. Nate Johnson for reviewing this thesis. I would like to thank the crew of the R.V. Blue Heron for their hard work collecting this data. I would like to thank Matt James for his help setting up the model during its infancy. The high speed computations would not be possible without the work of the Minnesota Supercomputing Institute, for that I am grateful. I thank the National Science Foundation for funding this research. Lastly, but certainly not least, this could not be possible without the love and support from my friends and family.

Abstract

Numerical models were used to investigate basic properties of near-inertial waves in large lakes. The Regional Oceanographic Modeling System (ROMS) was used to run a hierarchy of models to investigate the role wind stress (idealized and semi-realistic), thermal structure (isothermal and two layer), and bathymetry (flat bottom and spatially varying) have on near-inertial waves in lakes.

The currents produced by idealized forcing were compared with observations from the Lake Superior mooring array. The inertial response was found to be very sensitive to the duration of the impulse. Idealized wind stress acting for half an inertial period puts a substantial amount of energy into the inertial band of frequencies and little energy into other frequencies.

The first models considered were flat bottom square basins with closed boundaries and a two layer thermal structure. The inertial kinetic energy was weakest near the shore and was greatest near the center of the basin. Very little inertial kinetic energy was put into currents when using a uniform thermal structure. Modeling with periodic boundary conditions produced pure inertial oscillations in the upper mixed layer. No thermocline displacements were observed when using periodic boundary conditions, which shows that a transport divergence is necessary to initiate internal waves.

Lake Superior was modeled during the period of July 1, 2011 to September 19, 2011 and output from the model was compared with observations from the Lake Superior mooring array. A slow, approximately 30 day, counterclockwise rotation in the direction of wave propagation was observed in the model, which corroborates previous observations made in Lake Superior. Modeling suggests that near-inertial surface kinetic energy is enhanced over the Superior shoal, possibly due to a convergence of waves atop the shoal. The magnitude of the modeled currents agreed well with observations but phase did not. In order to accurately model near-inertial events in large lakes a higher resolution wind field may be needed and surface heat fluxes need to be included in the model.

Contents

List of Tables

List of Figures

Chapter 1

Introduction

1.1 Background

1.1.1 Internal Waves

The Norwegian explorer Fridtjof Nansen made the first observations of internal waves in 1893 while exploring the arctic. Nansen's ship, the Fram, had a reduced motion when sailing atop fresh water. The phenomenon, which Nansen called 'dead water', was a result of a internal wave at the interface between low density fresh water atop high density saline water. The details of the phenomenon were later explained by Ekman (1904).

Internal (gravity) waves occur at pycnoclines (density gradients) in a fluid. Two important pycnoclines in the ocean are the halocline (salinity gradient) and the thermocline (temperature gradient), the latter being more important in lacustrine environments. A buoyant force acts on a fluid parcel when it is displaced from equilibrium :

$$B = -g\Delta\rho \tag{1.1}$$

where g is the acceleration due to gravity, $\Delta\rho$ is the density difference between a parcel of water and the water surrounding it and B is the buoyant force per unit volume. The displacement from equilibrium also gives rise to a horizontal pressure gradient, which is the restoring force for a wave. These pressure gradients are also proportional to the density difference between the fluid parcel and the surrounding water, or air in the case of surface waves. Since the restoring force is proportional the density difference,

the restoring force for surface waves is greater than the restoring force for internal waves. The wavelength and period of internal waves span a wide range, centimeters to kilometers and seconds to hours respectively. The amplitude of internal waves can be orders of magnitude larger than surface gravity waves.

There is a whole classification of internal waves depending on the fluid stratification, wave amplitude, and generation mechanism. Interfacial waves propagate along withe interface separating fluids of difference densities. Standing waves in the atmosphere, termed lee waves or mountain waves, can form on the lee side (downwind side) of a mountain range. [1] This thesis will focus on near-inertial waves, which are waves whose dynamics are influenced by the Coriolis force when the wave frequency is comparable to the local inertial frequency.

The Coriolis effect [2] is an apparent deflection of a moving object in a rotating reference frame. The deflection will be to the right in the northern hemisphere and to the left in the southern hemisphere. The deflection is caused by the Coriolis force, which acts perpendicular to velocity and is only observed in a rotating reference frame. One way to observe the Coriolis effect is to have somebody throw a ball to you while you are a both on a playground roundabout. The ball will appear to be deflected away from you since you are on a rotating platform. However, somebody on the ground will observe the ball to move in a straight line. Even though the Coriolis force only has affects in the rotating reference frame it still behaves like a real force, i.e. it can an acceleration.

Two types of basin scale internal waves are typically observed in large lakes, namely Kelvin waves [3] and Poincaré waves [4] . Kelvin waves are shore hugging waves which have the most influence between the coast and a distance of about one Rossby radius. These waves propagate around the the basin of the lake and produce no flow normal to the shore. The amplitude decays off shore exponentially, $e^{(\frac{-fx}{c})}$, where f is the Coriolis frequency, x is the distance from shore, and c is the internal wave speed (Mortimer 1974). Poincaré waves on the other hand produce motion across the entire basin and have little effect near shore (Antenucci and Imberger 2001), this type of wave will be

[1] An example of a lee wave in the atmosphere is the so called "Sierra wave" that forms when winds lift off the Sierra Nevada mountain range.

[2] Named in honor of the Gaspard-Gustave Coriolis who wrote down the mathematical expression for the effect in 1835, but was not the first to recognize the effect (Graney 2011).

[3] Named in honor of William Thomson, Baron Kelvin of Largs, who first discovered these waves.

[4] Named in honor of Henri Poincaré who discovered these waves.

the focus of this thesis.

1.1.2 Near-Inertial Waves

Near-inertial waves (NIWs) are propagating Poincaré waves, i.e., the frequency is super-inertial but close to the inertial frequency. Long wavelength NIWs are commonplace in the ocean and have been estimated to be between 80 km - 180 km (Qi et al. 1995). The external and internal Rossby radius of deformation [5] define the length scale at which rotation becomes important for surface waves and internal waves respectively. The Rossby radius is defined as :

$$R = \frac{c}{f_o} \tag{1.2}$$

where c is the wave speed and f_o is the local inertial frequency. The external Rossby radius and internal Rossby radius for Lake Superior are approximately 350 km and 4 km respectively. [6] The internal Rossby radius was calculated assuming an epilimnion depth of 20 m, a hypolimnion depth of 130 m, and a density difference of 1kg m^{-3} across the metalimnion. Rotation will have little effect on surface gravity waves, since 350 km is comparable to the length of Lake Superior. Rotation will, however, have a significant effect on internal waves, since the internal Rossby radius is much smaller than the length of the basin.

NIWS are ubiquitous in the ocean and have been observed throughout the water column (Webster 1968). Coastal observations of near-inertial currents have been made by Shearman (2005) using the Coastal Mixing and Optics (CMO) mooring array [7] . Shearman (2005) found 10-20% of current variance can be attributed to the near-inertial band. The near-inertial band accounts for 80% of the variance when barotropic tidal variability is removed and the remaining variance is attributed to semi-diurnal internal tides. The vertical structure of velocity in the coastal ocean is dominated by the first baroclinic mode (Shearman 2005, Millot and Crépon 1981). Millot and Crépon (1981) observed that storm events generate inertial motion. Along with storm events, D'Asaro (1985) observed that moving cold fronts and moving low pressure systems generated

[5] named in honor of Carl-Gustaf Rossby.

[6] see Section 2.4 for the calculation of these values.

[7] The array consisted of four sites with instruments to measure physical properties of the water column.

inertial oscillations. He did this by comparing inertial events with synoptic weather charts.

Extensive observations of NIWs were made throughout the Laurentian Great Lakes in the 1960s and 1970s using moored platforms to collect data on the thermal and velocity structure. During the International Field Year for the Great Lakes (IFYGL) a comprehensive interdisciplinary study was done on Lake Ontario (McCulloch 1973). A staggered grid of moorings were placed throughout Lake Ontario (average spacing of 15 km), most stations recorded currents at 15 m and 30 m depth and temperature at 0 m, 10 m, 15 m, 30 m, and 50 m. The July 1972 thermal structure showed spectral energy at the inertial frequency (0.057 cycle hr^{-1}) to be greatest at the thermocline and that the spatially averaged velocity magnitude was greatest above the thermocline (Pickett and Richards 1975). A similar observation was made in Lake Erie (Boyce and Chiocchio 1987). Observations of winter (December 1972 - March 1973) currents in Lake Ontario at 15 m and 75 m depth showed inertial kinetic energy, calculated using the magnitude of the band-passed filtered velocity, to be greater during periods of stratification (Marmorino 1978). A similar study with 21 stations in Lake Huron showed that inertial motion was prominent during the stratified period of June-August 1966 and that this motion was clearly defined during periods of strong stratification (Sloss and Saylor 1976). In oceanic observations, Shearman (2005) observed a seasonality in the near-surface near-inertial kinetic energy. He observed near-inertial kinetic energy to be inversely proportional to stratification depth. In other words, as the thermocline deepens the near-surface near-inertial kinetic energy decreases. The baroclinic nature of NIWs in vertical velocity profiles has been observed in the coastal ocean (Shearman 2005) and lacustrine environments (Marmorino 1978). Blanton (1974) studied the seasonal variation of currents in 1970 throughout the water column in Lake Ontario and showed that inertial currents in the spring (May 16 - June 2), summer (July 4 - July 18), and fall (October 1 - October 19) accounted for about 20%, 50%, and 10% of the variance respectively at a site 16 km offshore. Blanton (1974) also showed that inertial energy decreases closer to shore. A decrease in near-inertial kinetic energy near the coast has also been observed on the New England shelf (Shearman 2005).

Recent observations in Lake Michigan and Lake Superior have corroborated the findings of these earlier studies. Choi et al. (2012) showed that NIWs were prominent

during the stratified season and accounted for about 80% of the surface observations at an open water site in Lake Michigan. Observations in Lake Superior from 2008-2011 show that the near-inertial response is related to the strength of stratification and that motion above and below the thermocline are roughly 180 degrees out of phase (Austin 2013). Austin (2013) analyzed NIWs as propagating plane waves and made estimates of the wave climate in Lake Superior. He found the wavelength to vary between 30-60 km and the group speed (speed energy is transferred) to be around 22 cm s^{-1}. An interesting finding made by Austin (2013) was that the direction of these waves slowly veers counterclockwise with a period of about 1 month, which he noted has the same direction and period as the lowest order internal Kelvin wave.

The spatial structure of NIWs is not well characterized and many previous studies have approached the problem with modal analysis (Schwab 1977, Rueda et al. 2003, Gómez-Giraldo et al. 2006, Ahmed et al. 2013). (Schwab 1977) used a numerical procedure to calculate the amplitude and phase distribution of three Poincaré type modes in Lake Ontario. Schwab (1977) calculated the three lowest Poincaré modes to have periods of 16.8, 16.7, and 16.6 hours. A peak centered at these periods was observed by Pickett and Richards (1975) in the average power spectra of temperature. However, Pickett and Richards (1975) observed spectra of velocity components to be closer to the inertial period (17.35 hours). Schwab (1977) suggested it would be hard to separate these modes by standard methods and that the observed temperature spectra most likely contained energy from a few modes. Numerical modeling in Lake Michigan by Ahmed et al. (2013) show the spatial structure of dominant internal modes. Analysis of isothermal displacements revealed three nodes in Lake Michigan with clockwise phase propagation around each node. However, modeling studies have suggested that the spatial structure of internal waves is too complex to be predicted by internal wave modes and that bathymetry plays an important role in the spatial distribution of energy (Rueda et al. 2003).

The partition of energy in NIWs has been of particular interest in Lake Kinneret (Sea of Galilee) (Antenucci and Imberger 2001). Potential energy is stored in undulations of pycnoclines, while kinetic energy is carried in the currents. Large currents are observed in the top mixed layer while weaker currents are observed below the thermocline. This is because the wind stress directly acts on the mixed layer producing larger

currents. However, the magnitude of velocity does depend on the relative thickness of the epilimnion and hypolimnion. When the surface water subsides, such as at a coast, the thermocline will be depressed generating a weak return flow in the bottom layer. The resulting oscillations at the thermocline are analogous to surface gravity waves. Numerical solutions show that downward propagation of energy from the upper layer to the bottom layer is accompanied by an upward phase propagation (Kundu et al. 1983). The ratio of potential to kinetic energy in NIWs is dependent on the Burger number [8] defined as :

$$Bu = \left(\frac{R}{L}\right)^2 \tag{1.3}$$

where R is the Rossby radius of deformation and L is the length scale of the basin (Antenucci and Imberger 2001). Antenucci and Imberger note that high Burger number basins have equal partition between potential and kinetic energy while low Burger number basins, such as Lake Superior, have an energy partition dominated by kinetic energy. The Burger number for Lake Superior is $Bu = (\frac{R_i}{L})^2 = (\frac{4 \text{ km}}{250 \text{ km}})^2 = 2.3 * 10^{-3}$, where R_i is the internal Rossby radius, therefore near-inertial energy will be predominantly kinetic in Lake Superior.

1.2 Motivation

The motivation for this thesis stems from the proposed connection between NIWs and the resuspension of sediment during the stratified season. Near-inertial currents have been correlated with the thickness of the benthic nepheloid layer, suggesting that these waves are important drivers resuspending nutrients and sediment (Hawley 2004). Also, autonomous glider observations in Lake Superior show a link between stratification and backscatter (Austin 2013). Therefore, understanding the spatial distribution of near-inertial energy could have ecological significance. Along with resuspending sediment, NIWs can also move oxygen across the thermocline (Bouffard et al. 2014) . The approach taken in this thesis will follow Austin (2013) and analyze NIWs in terms of the wave climate due to the complex nature of modal analysis for irregular basins.

The other motivating factor for this study is to better understand the relationship between the wind field and near-inertial wave energy. One dimensional models (Pollard

[8] Named in honor of Alewyn Burger.

1970, Pollard and Millard Jr. 1970) were able to show a few important relationships between the wind field and NIWs. The first relationship is that a wind stress acting for less than one inertial period effectively puts energy into inertial motions (Pollard 1970). Imagine a top-hat wind stress acting for one inertial period, the amount of energy put into near-inertial currents during the first half will be taken out during the second half. Therefore, a wind stress acting for half an inertial period effectively puts the most energy into the near-inertial currents. Secondly, a wind stress rotating clockwise in the northern hemisphere (counter-clockwise in the southern hemisphere) has the potential to continuously increase the magnitude of the velocity (Pollard and Millard Jr. 1970). For example, if the wind stress were rotating at the inertial frequency then the direction of the wind stress and direction of the current would always be the same and therefore momentum could always be put into the motion. This has been shown in observations as well, Boyce and Chiocchio (1987) presented observational evidence that large near-inertial events are associated more with clockwise rotating wind vectors than the amplitude of the wind stress. Modern models do not have the predictive power to determine when and where large inertial events will occur and it is hoped that someday these models can make accurate predictions.

1.3 Lake Superior

Lake Superior formed approximately 11,000 years ago as the Laurentide ice sheet retreated northeastward across what is now Canada (Thomas and Dell 1978). Lake Superior is part of the Laurentian Great Lakes System, which also includes Lake Huron; Lake Ontario; Lake Michigan; and Lake Erie. Superior is the largest freshwater lake of the Laurentian Great Lakes by surface area (82,100 km^2) and volume (12,100 km^3).

Worldwide, Lake Superior is the largest lake by surface area and third largest by volume. The lake is an important water source and holds approximately 10% of the world's freshwater supply. Lake Superior has a length of 560 km, and breadth of 260 km. The retention time of the lake is about 200 years (Quinn 1992). The lake is home to 38 native species of fish, including ciscoes, whitefish, and trout.

Lake Superior can be divided into two deep basins separated by a relatively shallow ridge off the Keweenaw peninsula (Figure 1.1). The average depth of the lake is about

150 m and has a maximum depth of 406m (Schwab and Sellers 1996).

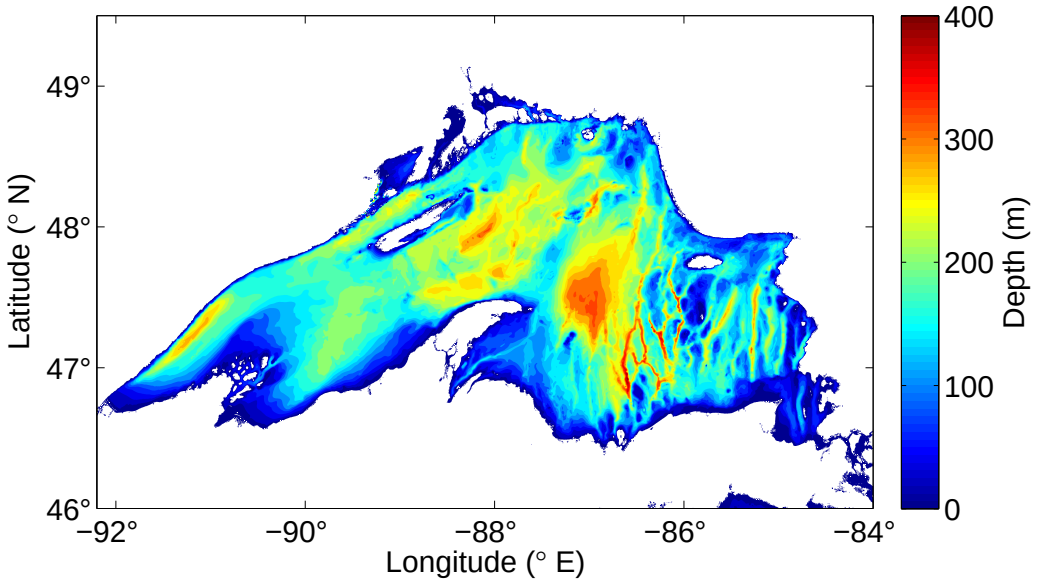

Figure 1.1: **Lake Superior Bathymetry.** Lake Superior has a mean depth of 150 m and a maximum depth of 406 m. A shallow ridge extending off the Keweenaw Peninsula separates the lake into two deep basins (NOAA).

1.3.1 Thermal Structure

Lake Superior is a dimictic lake and therefore stratifies twice per year, once in summer and once in winter (Figure 1.2). Water has a unique relationship with temperature in that the temperature of maximum density (T_{md}) is greater than the freezing point (T_f) (Figure 1.3). At zero gauge pressure T_{md}=3.98°C and T_f=0°C. T_{md} decreases as pressure increases therefore, T_{md} is lower at greater depth. During the summer stratified period the bottom water remains close to the temperature of maximum density.

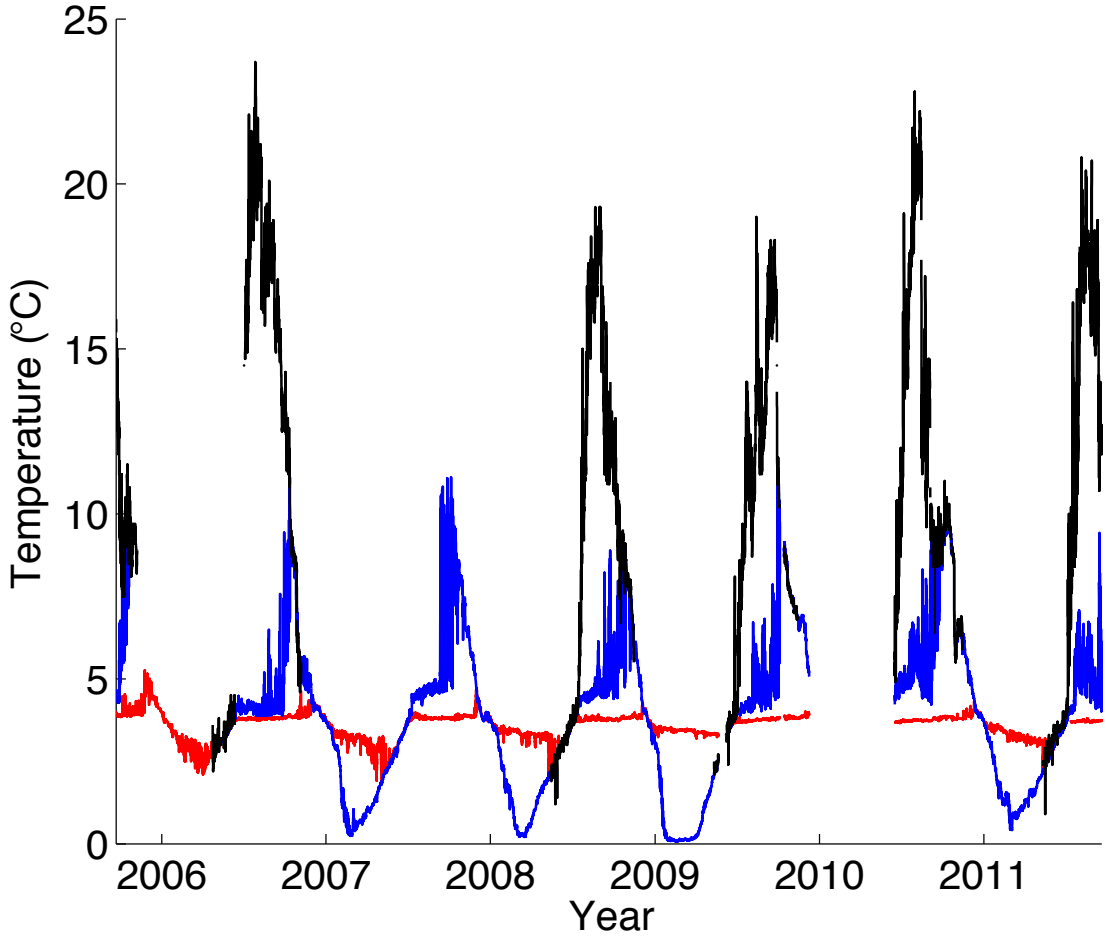

Figure 1.2: **Lake Superior Thermal Structure.** Thermal structure of Lake Superior over the course of 6 years. The black, blue, and red lines represent the water temperature at 1m, 25-37m, and 120-180m below the surface respectively.

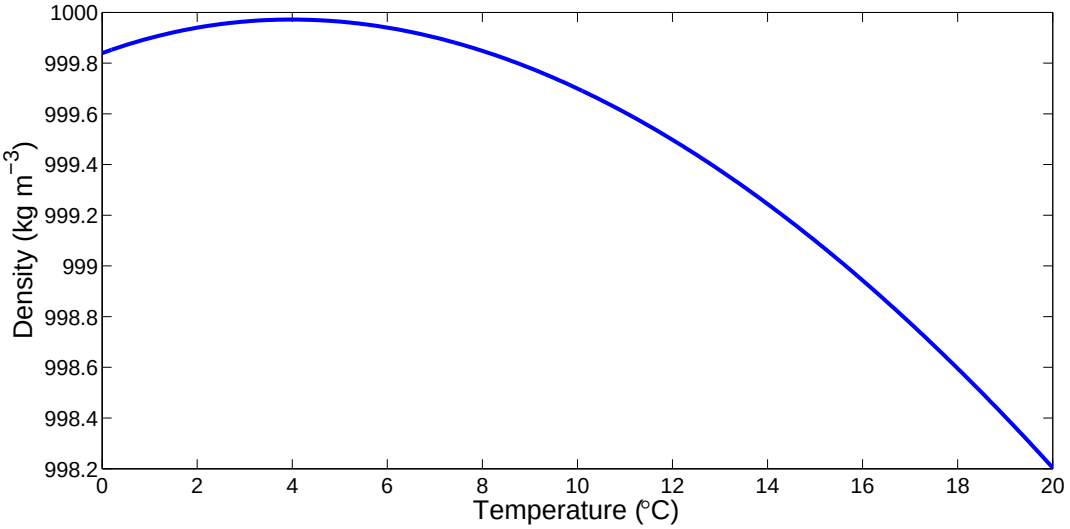

Figure 1.3: **Freshwater Density.** Fresh water density as a function of temperature at zero gauge pressure (Chen and Millero 1986).

Weather conditions set up thermal stratification in lakes. Lets assume the entire water column is at T_{md}, surface heat fluxes will then cause the surface of the lake to warm or cool away from T_{md} and this less dense water will float atop the more dense water below. Water nearest to the bottom of the lake will remain very close to T_{md} throughout the entire year. The water column will separate into two distinct layers as more and more heat is exchanged with the surface of lake. These layers are termed the epilimnion (surface mixed layer) and the more stagnant hypolimnion below. At the intersection between these two layers is the metalimnion, which is characterized by the thermocline or sharp temperature/density gradient. As the epilimnion heats up the density difference between the two layers increases, leading to a steeper and more stable thermocline.

The hypolimnion becomes enriched with oxygen during the spring mixing when the lake is isothermal. When stratification sets in, the epilimnion acts as a barrier to the hypolimnion and the deep water is cut off from oxygen exchange with the atmosphere. The hypolimnion can become anoxic as oxygen is consumed by anaerobic decomposition. However, this is not a problem for Lake Superior (Niirnberg 1995). During stratification

the lake can partially mix due to high wind speeds.

The beginning of stratification varies around the lake, typically late June near the shore and mid-July in open water. November is typically the end of the stratified season. It is likely to expect stratification to start earlier and have a prolonged period of stratification as the global temperature increases (Austin and Colman 2007). Negative stratification occurs in the winter as the epilimnion cools below the temperature of maximum density. During winter stratification, the bottom water remains close to the temperature of maximum density and the top layer is close to the freezing temperature. Although the density difference between the epilimnion and hypolimnion in the winter is very small, it is enough to change the dynamics of the water column. During the summer stratified season the density difference between the surface and bottom is close to $20 * 10^{-4}$g cm^{-3} while during winter stratification the density difference is around $5 * 10^{-4}$g cm^{-3}.

Chapter 2

Mathematical background

2.1 Navier-Stokes Equations

The Navier-Stokes equations [1] are a set of partial differential equations that define the motion of a parcel of fluid. Solutions to these equations define the velocity field at a particular time and point in space. The equations are derived by applying Newton's second law to a fluid parcel, see Kundu and Cohen (2008) for a derivation. These equations are important in any situation that has fluid flow, such as modeling currents in the ocean or the dynamics of an aircraft. These equations were introduced in the 19th century and are still relevant today in a practical and academic sense. In a rotating reference frame the Navier-Stokes equations are defined in vector notation as :

$$\rho(\frac{\partial \vec{V}}{\partial t} + \vec{\vec{V}} \bullet \nabla\vec{V}) = -\nabla P - \rho(2(\vec{\Omega} \times \vec{V})) - \rho\vec{g_n} - \rho\vec{\Omega} \times (\vec{\Omega} \times \vec{R}) + \mu\nabla^2\vec{V} \qquad (2.1)$$

See Table (2.1) for a definition of each term in equation (2.1).

[1] Honoring Claude-Louis Navier and George Gabriel Stokes.

Table 2.1: Definition of variables in the Navier-Stokes equations.

Term	**Description**
$\vec{V}$	Velocity vector : $\vec{V} = u\hat{i} + v\hat{j} + w\hat{k}$
$\vec{R}$	Displacement vector : $\vec{R} = x\hat{i} + y\hat{j} + z\hat{k}$
ρ	Fluid density
$\frac{\partial \vec{V}}{\partial t}$	Acceleration of fluid parcel
$\vec{V} \bullet \nabla \vec{V}$	Convective acceleration
∇P	Pressure gradient
$2(\vec{\Omega} \times \vec{V})$	Coriolis acceleration
$\vec{\Omega} \times (\vec{\Omega} \times \vec{r})$	Centrifugal acceleration
$\mu \nabla^2 \vec{V}$	Shear stress
$\vec{g_n}$	Newtonian gravitational acceleration
Ω	Rotation rate of Earth

The reference frame is oriented so positive $\hat{i}$ is to the east, positive $\hat{j}$ is to the north, and positive $\hat{k}$ is upward and pointing away from the surface of the Earth. Two terms in Equation (2.1) arise because observations are made from a rotating, or non-inertial, reference frame. These terms are the Coriolis acceleration ($2(\vec{\Omega} \times \vec{V})$), and the centrifugal [2] acceleration ($\vec{\Omega} \times (\vec{\Omega} \times \vec{R})$). The centrifugal acceleration is an apparent acceleration that is evoked in a non-inertial (accelerating) reference frame. The centrifugal acceleration balances the centripetal [3] acceleration. To simplify the Equation (2.1) the centrifugal acceleration vector can be added to gravitational acceleration vector to define an affective gravitational acceleration ($-\vec{g} = -\vec{g_n} - \vec{\Omega} \times (\vec{\Omega} \times \vec{R})$). The Coriolis acceleration gives rise to an apparent deflection of an object when it is moving; this deflection is to the right of the velocity in the northern hemisphere and to the left of the velocity in the southern hemisphere. The components of the Coriolis acceleration are defined as :

[2] Latin for "center fleeing".
[3] Latin for "center seeking".

$$2(\vec{\Omega} \times \vec{V}) = 2\Omega\sin(\phi)v\hat{i} - 2\Omega\sin(\phi)u\hat{j} \tag{2.2}$$

$$= -fv\hat{i} + fu\hat{j} \tag{2.3}$$

where $f = 2\Omega\sin(\phi)$ is the inertial frequency [4] , $\Omega = \frac{2\pi}{\text{day}}$ is the rotational frequency of Earth, ϕ is latitude, u and v are the zonal and meridional components of the velocity respectively. The inertial period is given by $T = \frac{2\pi}{f}$. At $46.7°N$ latitude, the approximate location of Duluth, Minnesota, $f \approx 1.1 * 10^{-4}\text{s}^{-1}$ and the inertial period is $T \approx 16$ hrs. The physical meaning of the inertial frequency will be discussed in section (2.2).

Shear stresses, such as molecular friction ($\nu\nabla^2\vec{V}$), produce rotational motion which can be assumed negligible, at least in the ocean. The relative of importance of this term in the Navier-Stokes equation can be quantified by the Reynolds number [5] , a dimensionless number defined as the ratio of inertial forces to viscous forces :

$$Re = \frac{UL}{\nu} \tag{2.4}$$

where U is a typical flow speed, L is the typical length scale, and ν is the kinetic viscosity. A typical Reynolds value for open water in Lake Superior is $Re = \frac{(0.05\ ms^{-1})2*10^2m}{1m^2s} = 10^8$, a large Reynolds number implies that molecular friction can be neglected in the Navier-Stokes equation. Lastly, the local acceleration and advective acceleration can be combined into one term, the total acceleration, ($\frac{d\vec{V}}{dt} = \frac{\partial\vec{V}}{\partial t} - \vec{\vec{V}} \bullet \nabla\vec{\vec{V}}$). After all of these simplifications equation (2.1) can be written concisely as :

$$\rho\frac{d\vec{V}}{dt} = -\nabla P - \rho(2(\vec{\Omega} \times \vec{V})) - \rho\vec{g} \tag{2.5}$$

Equation (2.5) will from henceforth be referred to as the Navier-Stokes equation.

2.2 Pure Inertial Oscillations

Lets consider a parcel of water which is only affected by the Coriolis force. Pressure gradients and gravity will be neglected in equation (2.5), since there will be no displacement at the surface. The Navier-Stokes equation then simplifies to :

[4] The inertial frequency, f, is sometimes termed the Coriolis frequency or Coriolis parameter.

[5] Named in honor of Osbourne Reynolds, who popularized its use. However, the concept of the number is credited to Stokes (Rott 1990).

$$\frac{d\vec{V}}{dt} = -(2(\vec{\Omega} \times \vec{V})) \tag{2.6}$$

$$\frac{du}{dt}\hat{i} + \frac{dv}{dt}\hat{j} = fv\hat{i} - fu\hat{j} \tag{2.7}$$

The component form of equation (2.7) is :

$$\frac{du}{dt} - fv = 0 \tag{2.8}$$

$$\frac{dv}{dt} + fu = 0 \tag{2.9}$$

where f is the inertial frequency, u is the zonal (east-west) component of the velocity and v is the meridional (north-south) component of velocity. Equation (2.8) is the x component and equation (2.9) is the y component of the momentum equation. Solving these equations for each velocity component and position component yields : [6]

Velocity Components	**Position Components**
$u(t) = u_o \cos(ft + \phi)$	$x(t) = \frac{u_o}{f} \sin(ft + \phi)$
$v(t) = -u_o \sin(ft + \phi)$	$y(t) = \frac{u_o}{f} \cos(ft + \phi)$

Physically, these equations define a parcel of water moving in a circle of radius $\frac{u_o}{f}$ at a frequency f. The inertial frequency represents the angular frequency of an object acted on solely by the Coriolis force. Since there is no movement of the surface, the pure inertial oscillation case corresponds to the impossible scenario of a wave having an infinite wavelength. However, motion in the open ocean is close to pure-inertial. Also, notice that the magnitude of the velocity does not change with time, which implies that the Coriolis force acts perpendicular to the velocity vector and only acts to change the direction of velocity but not the magnitude. A simple proof of this is provided below.

[6] For a derivation see appendices (A.1).

$$u(t) = \sqrt{u^2 + v^2} \tag{2.10}$$
$$= \sqrt{u_o^2 \cos(ft+\phi)^2 + (-u_o)^2 \sin(ft+\phi^2)} \tag{2.11}$$
$$= \sqrt{u_0^2(\cos(ft+\phi)^2 + \sin(ft+\phi)^2)} \tag{2.12}$$
$$= u_o \tag{2.13}$$

This shows that the speed of the fluid parcel is independent of time

2.3 Poincaré Waves - Single Layer

This time we will allow the free surface to oscillate in a fluid of uniform density, (Figure 2.1).

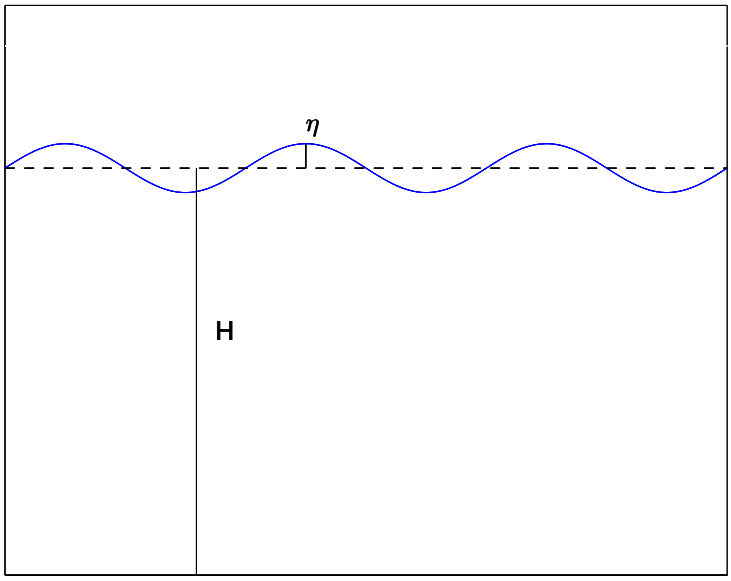

Figure 2.1: **single-layer diagram.** A diagram of a fluid where the surface is allowed to oscillate. H represents the depth of the water and and η represents the surface elevation from equilibrium

The Navier-Stokes equation for this situation can be written as :

$$\rho\frac{d\vec{V}}{dt} = -\nabla P - \rho(2(\vec{\Omega}\times\vec{V})) - \rho\vec{g} \tag{2.14}$$

Lets substitute $\nabla P = \nabla\rho g\eta$ into equation (2.14) :

$$\rho\frac{d\vec{V}}{dt} = -\nabla P - \rho(2(\vec{\Omega}\times\vec{V})) - \rho\vec{g} \tag{2.15}$$

$$\rho\frac{d\vec{V}}{dt} = -\rho g\nabla\eta - \rho(2(\vec{\Omega}\times\vec{V})) - \rho\vec{g} \tag{2.16}$$

$$\frac{d\vec{V}}{dt} = -g\nabla\eta - (2\vec{\Omega}\times\vec{u}) - \vec{g} \tag{2.17}$$

$$\frac{du}{dt}\hat{x} + \frac{dv}{dt}\hat{y} + \frac{dw}{dt}\hat{z} = -g\frac{d\eta}{dx}\hat{x} - g\frac{d\eta}{dy}\hat{y} - g\frac{d\eta}{dz}\hat{z} + fv\hat{x} - fu\hat{y} - g\hat{z} \tag{2.18}$$

Equation (2.18) can be broken down into components and written as :

$$\frac{du}{dt} - fv = -g\frac{d\eta}{dx} \tag{2.19}$$

$$\frac{dv}{dt} + fu = -g\frac{d\eta}{dy} \tag{2.20}$$

$$\frac{dw}{dt} + g = -g\frac{d\eta}{dz} \tag{2.21}$$

Where $u, v,$ and w are the zonal, meridional, and vertical velocity components respectively, g is the gravitational acceleration, and η is the free surface displacement.

A plane wave solution of the following form was applied to Equations (2.19 -2.18) :

$$(u, v, \eta) \sim (u_o, v_o, \eta_o)\exp i(\vec{K}\bullet\vec{R} - \omega t) \tag{2.22}$$

The wave vector, or vector extension of the wave number, can be written as $\vec{K} = [k_x; k_y; k_z]$. Without loss of generality, we will assume the wave is solely propagating in the x direction.

The resulting dispersion relation and velocity field are as follows : [7]

$$\omega_{BT}^2 = f^2 + gHk^2 \tag{2.23}$$

[7] For a derivation see appendices (A.2).

Velocity Components

$$u(t) = \frac{\omega}{hk}\eta_o \cos(kx - \omega t)$$
$$v(t) = \frac{f}{hk}\eta_o \sin(kx - \omega t)$$

Position Components

$$x(t) = -\frac{\eta_o}{hk}\sin(kx - \omega t)$$
$$y(t) = \frac{f}{hk\omega}\eta_o \cos(kx - \omega t)$$

Free Surface Displacement

$$\eta(t) = \eta_o \cos(kx - \omega t)$$

Equation (2.23) is the barotropic (depth independent) dispersion relationship and implies that f sets a lower limit to the frequency of a gravity wave.

2.4 Poincaré Waves - Double Layer

Now lets consider a two layer fluid where a less dense fluid overlies a more dense fluid. The density of the fluid in each layer will be assumed constant throughout, i.e. pressure and temperature effects on density will be ignored. This scenario has two interfaces which can oscillate , the air-water interface and an internal interface separating the two fluid layers, Figure (2.2). The Navier-Stokes equation can be applied separately to each layer.

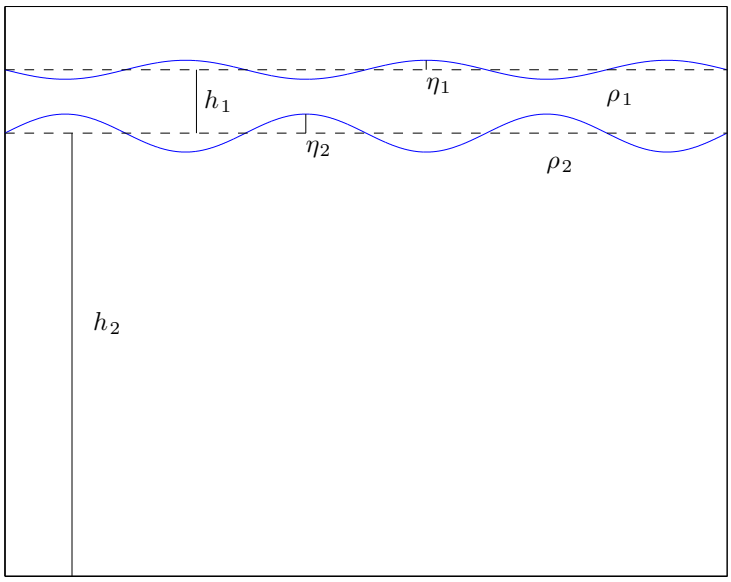

Figure 2.2: **two-layer diagram.** h_1 will be the depth of the top layer and h_2 will be the depth of the bottom layer. The densities in each layer are given by ρ_1 and ρ_2, where $\rho_2 > \rho_1$. The interface displacements are given by η_1 and η_2 where $\eta_2 >> \eta_1$.

Top Layer	**Bottom Layer**
$\frac{du_1}{dt} - fv_1 = -g\frac{d\eta_1}{dx}$	$\frac{du_2}{dt} - fv_2 = -g'\frac{d\eta_2}{dx} - g\frac{d\eta_1}{dx}$
$\frac{dv_1}{dt} + fu_1 = -g\frac{d\eta_1}{dy}$	$\frac{dv_2}{dt} + fu_2 = -g'\frac{d\eta_2}{dy} - g\frac{d\eta_1}{dy}$
$h_1(\frac{du_1}{dx} + \frac{dv_1}{dy}) + \frac{d\eta_1}{dt} - \frac{d\eta_2}{dt} = 0$	$h_2(\frac{du_2}{dx} + \frac{dv_2}{dy}) + \frac{d\eta_2}{dt} = 0$

A rigid lid approximation was assumed which neglects variations of the air-water interface and assumes that the surface behaves as if it is immobile or a "rigid lid." However, pressure gradients are still produced even with this approximation. Applying the same plane wave solution as in equation (2.22) to this two layer system yields the following dispersion relation and velocity field :

$$\omega_{BC}^2 = f^2 + g'h'k^2, \quad \text{where} \quad g' = g\frac{\Delta\rho}{\rho_o}, \quad h' = \frac{h_1 h_2}{h_1 + h_2} \tag{2.24}$$

Top Layer Solutions

$$u_1 = u_{10}\cos(kx - \omega t)$$
$$v_1 = \frac{f}{\omega}u_{10}\sin(kx - \omega t)$$

Bottom Layer Solutions

$$u_2 = -\frac{h_1}{h_2}u_{10}\cos(kx - \omega t)$$
$$v_2 = -\frac{h_1}{h_2}\frac{f}{w}u_{10}\sin(kx - \omega t)$$

Free Surface Displacement

$$\eta_1 = 0$$
$$\eta_2 = -\frac{h_1 k}{\omega}u_{10}\cos(kx - \omega t)$$

Since there are two layers there are two modes of oscillation, one which is depth independent and one which is depth dependent. The barotropic mode, ω_{BT}^2, is the depth independent mode and corresponds to the two layers moving in phase which each other. The system behaves as a homogenous fluid, as if there is no internal interface. The depth dependent mode, or baroclinic mode ω_{BC}^2, corresponds to the two interfaces moving out of phase with each other. When the surface layer is depressed the bottom layer is at its peak. However, assuming a rigid lip approximation will only yield the baroclinic mode of oscillation.

The Rossby radius of deformation defines a length scale when the Earth's rotation becomes important. The external Rossby radius of deformation defines the length scale at which rotation affects barotropic frequencies and the internal Rossby radius defines when rotation affects baroclinc frequencies. These values are quantified below assuming $g' = g\frac{\Delta\rho}{\rho_o} = 9.8\ \text{ms}^{-2}\frac{1\ \text{kgm}^{-3}}{1000\ \text{kgm}^{-3}} = 0.0098$ and $h' = \frac{h_1 h_2}{H} = \frac{20m130m}{150m} = 17.3$ m.

ExternalRossby Radius

$$\begin{aligned} Re_e &= \frac{C}{f} \\ &= \frac{\sqrt{gH}}{f} \\ &= \frac{\sqrt{9.8\text{ms}^{-2}150\text{m}}}{1.1 * 10^{-4}\text{s}^{-1}} \\ &= 350\ \text{km} \end{aligned}$$

Internal Rossby Radius

$$\begin{aligned} Re_i &= \frac{C}{f} \\ &= \frac{\sqrt{g'h'}}{f} \\ &= \frac{\sqrt{9.8\text{ms}^{-2} * 0.001 * 17.3\text{m}}}{1.1 * 10^{-4}\text{s}^{-1}} \\ &= 4\ \text{km} \end{aligned}$$

The barotropic response of the lake will be weak since the external Rossby radius is comparable to the length scale of the Lake Superior basin (250 km). Conversely, the internal Rossby radius is much smaller than the length scale of Lake Superior, suggesting that NIWs will be dominated by a baroclinic mode.

Chapter 3

Methods

3.1 Modeling

A hierarchy of simulations were used to explore the effects of wind duration and bathymetry on the spatial distribution of near-inertial energy. Three basins were considered :

- Square (200 km x 200 km) basin with uniform bathymetry.
- Lake Superior basin with uniform bathymetry.
- Lake Superior basin with realistic bathymetry

Two thermal structures were explored, a homogenous thermal structure of 4°C and a two layer structure. Two types of forcing were explored, a spatially uniform top-hat wind stress and a spatially/temporally varying wind stress.

3.1.1 Configuration

The regional oceanographic modeling system (ROMS) is a three-dimension, free-surface, terrain-following numerical model that solves the Reynolds-averaged (time-averaged) Navier-Stokes equations using the hydrostatic and Boussinesq assumptions. The hydrostatic assumption assumes the vertical pressure force is balanced by the weight of the fluid parcel. In which case, the pressure at a given depth is given by the hydrostatic equation, $\frac{\partial P}{dz} = -\rho g$. The Boussinesq approximation assumes that density variations are negligible in the Navier-Stokes equations, except for the buoyancy term where ρ is

multiplied by g. The non-linear equations of motion are solved using a predictor(leap-frog)-corrector(Adam-Moulton) finite difference scheme. To solely look at the effects of surface stress and stratification on near-inertial energy, the model was configured for no surface heat fluxes. No surface heat fluxes implies that the the heat content of the lake remains constant.

Lake Superior was modeled as closed basin with no inflows or outflows, since the time scale of internal waves in Lake Superior is five orders of magnitude less than than the residence time. The bathymetry used has a spatial resolution of 2km (Schwab and Sellers 1996) and was smoothed with the following three point moving average :

$$x_t = 0.25x_{t-1} + 0.5x_t + 0.25x_{t+1} \tag{3.1}$$

until the Beckman and Haidvogel number was less than 0.8. A Beckman and Haidvogel number less than unity ensures model stability and avoids spurious deep water currents. This number is defined as follows :

$$R_x = \max \frac{|h(i) - h(j)|}{h(i) + h(j)} \tag{3.2}$$

where $h(i)$ and $h(j)$ is the depth at neighboring grid cells and R_x is the Beckman and Haidvogel number.

ROMS was configured using an f-plane approximation (constant inertial frequency), since Lake Superior spans about 2.5 degrees of latitude and small variations in f are assumed to be negligible. The inertial frequency in Lake Superior varies between 1.055 10^{-4} s^{-1} and 1.098 10^{-4} s^{-1}, assuming latitudes of 46.5° and 49° respectively. The Mellor-Yamada closure scheme was used, which takes eddy viscosity into account and estimates turbulence on scales which can not be resolved by the model. The output from each model was linearly interpolated onto a common grid. One implication of this is that current velocities one grid cell away from the coast must be discarded since the interpolation used points outside the basin. The model used an Arakawa C grid (Figure 3.1), which is best used for fine resolutions (<50km).

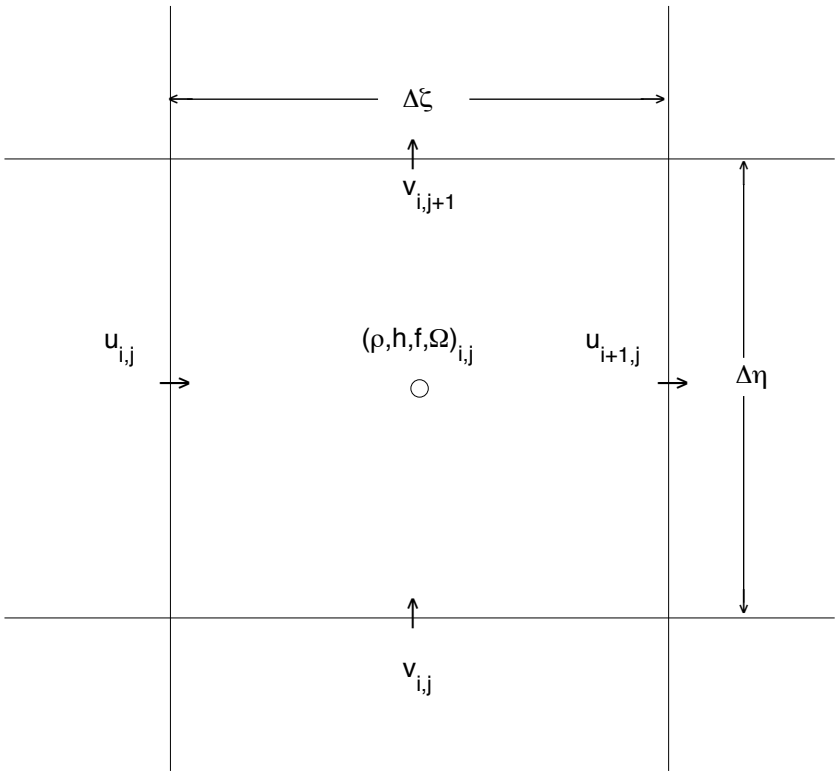

Figure 3.1: **Arakawa-C Grid Cell.** The Arakawa-C grid cell computes density, depth, and inertial frequency at the center of each cell. The u and v component of the velocity are computed half a cell distance away. $\Delta\eta$ and $\Delta\zeta$ are the resolution of the model in the meridional and zonal direction respectively.

The model used a time step of Δt =200 seconds and data was output hourly. Since ROMS uses a time split-explicit algorithm the depth integrated equations were time stepped at $\Delta t = \frac{200}{30}$ seconds. For stability, the CFL (Courant-Friedrichs-Lewy) condition requires the courant number to be less than unity everywhere in the model. The CFL condition can be expressed as :

$$\left| \frac{V \Delta t}{\Delta x} \right| \leq 1 \tag{3.3}$$

where V is the maximum internal wave speed, Δt is the internal time step and Δx is the horizontal spatial resolution. It is easy to show that the CFL condition holds at the deepest point in the model (350 m) by calculating the courant number for a wave at

the surface and at the internal interface.

External Courant Number

$$\frac{V_{external}\frac{\Delta t}{30}}{\Delta x}$$

$$\frac{\sqrt{gH_{max}}\frac{\Delta t}{30}}{\Delta x}$$

$$\frac{\sqrt{9.8\ \text{ms}^{-2} * 350\ \text{m}} * \frac{200\ \text{s}}{30}}{2000\ \text{m}}$$

$$0.20 < 1$$

Internal Courtant Number

$$\frac{V_{internal}\Delta t}{\Delta x}$$

$$\frac{\sqrt{g'h'}\Delta t}{\Delta x}$$

$$\frac{\sqrt{9.8\ \text{ms}^{-2} * 0.001 * \frac{20\ \text{m} * 330\ \text{m}}{350\ \text{m}}} * 200\ \text{s}}{2000\ \text{m}}$$

$$0.04 < 1$$

This shows that the model is likely to be stable if $\Delta x = 2000$ m, $\Delta t = 200$ s, the maximum water depth is less than 350 m, and the thermocline depth is less than 20 m. The CFL condition ensures material is not advected through a grid cell in the model time step. The CFL condition is required, but not sufficient, for model stability. More information on model stability can be found in Glover et al. (2011).

3.1.2 Vertical Structure

ROMS is a sigma level model, meaning that the vertical grid resolution is proportional to the water depth, which was configured for 30 vertical layers staggered throughout the water column. The spacing between each vertical level varied between 0.2 m near the top and 15 m at the bottom (Figure 3.2). The vertical stretching was given by :

$$C(\sigma) = \frac{1 - \cosh(\theta_s \sigma)}{\cosh(\theta_s) - 1} \tag{3.4}$$

where $\theta_s = 3$, $\sigma = \frac{n-N-0.5}{N} \quad n = 1 \ldots N$, where N is the total number of vertical layers, and n represents the vertical layer that is being stretched.

Two types of thermal structures were used, a uniform thermal structure and a stratified (two layer) thermal structure. The well mixed water column was chosen to be $4°C$, since it is close to T_{md}. The two layer system was modeled using the following expression :

$$T(z) = T_{bot} + \left(\frac{T_{top} - T_{bot}}{2}\right) * (1 + \tanh\left(\frac{z + z_{cline}}{s}\right)) \tag{3.5}$$

Where T_{bot} is the temperature of the bottom layer (hypolimnion), T_{top} is the temperature of the top layer (epilimnion), z_{cline} is the thermocline depth, and s is a thermocline thickness parameter. Table (3.1) outlines the values used in Equation 3.5.

Table 3.1: Two Layer Thermal Structure Values

Parameter	**Value**	**Description**
T_{bot}	$4°C$	Bottom layer temperature
T_{top}	$21\ °C$	Top layer temperature
z_{cline}	20 m	Thermocline depth
s	2	Thermocline thickness parameter

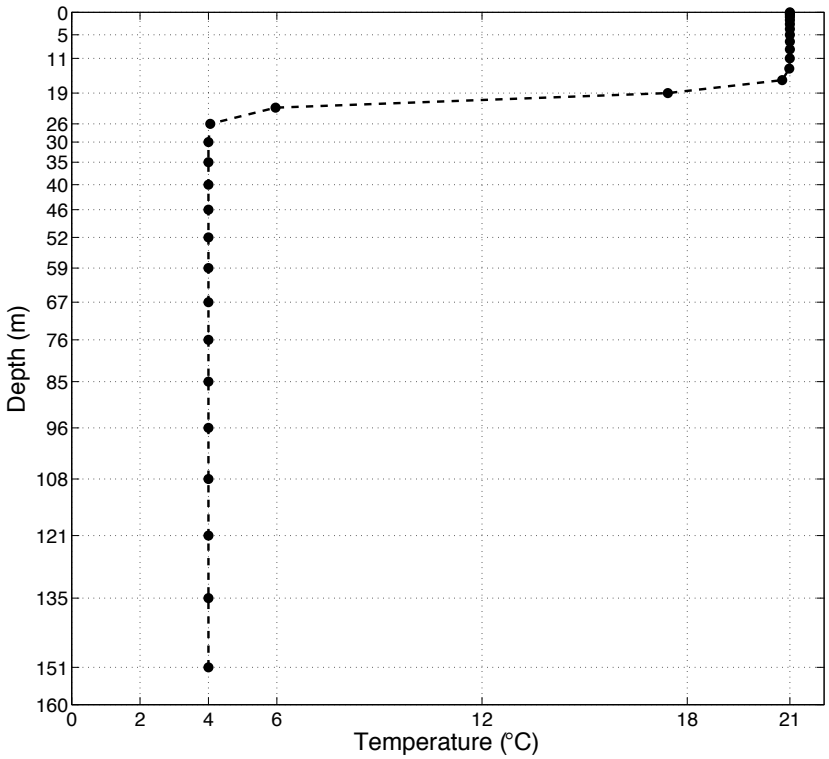

Figure 3.2: **Modeled Initial Thermal Structure.** The initial thermal structure for a point where the max depth is 160m.

3.1.3 Forcing

Two types of forcing were used, an impulse of wind stress (idealized forcing) and temporally / spatially varying wind stress. The idealized forcing was a spatially uniform pulse of wind stress with a magnitude of 0.1 Nm^{-2} directed to the east; this is equivalent to a wind speed of 8 ms^{-1} at 10 m above the surface (Fairall et al. 1996). To maximize the energy input at the inertial frequency the duration of the wind pulse lasted for half an inertial period (Boyce et al. 1989).

Temporally and spatially varying wind stress was derived from the North American Regional Reanalysis (NARR) climatology data. This is an extension of National Centers for Environmental Prediction (NCEP) Global Reanalysis which runs models of the North American region. NARR provides high resolution (32km spatial / 45 layers) climatology model output from 1979 up to today with a temporal resolution of 3 hours. The zonal and meridional wind speeds at 10 m above the surface from 2011 were used to compute the wind stress at the surface. The sign convention used for u is positive (+) for winds from the west blowing to the east and negative (-) for winds from the east blowing to the west. The v component is positive for winds from south blowing north and negative for winds from north blowing south. The modeled wind stress was linearly interpolated to an hourly time grid and objective analysis was used to interpolate the output onto a 2 km x 2 km grid. The magnitude of the wind stress derived from NARR wind speeds shows large spatial and temporal variability (Figure 3.3).

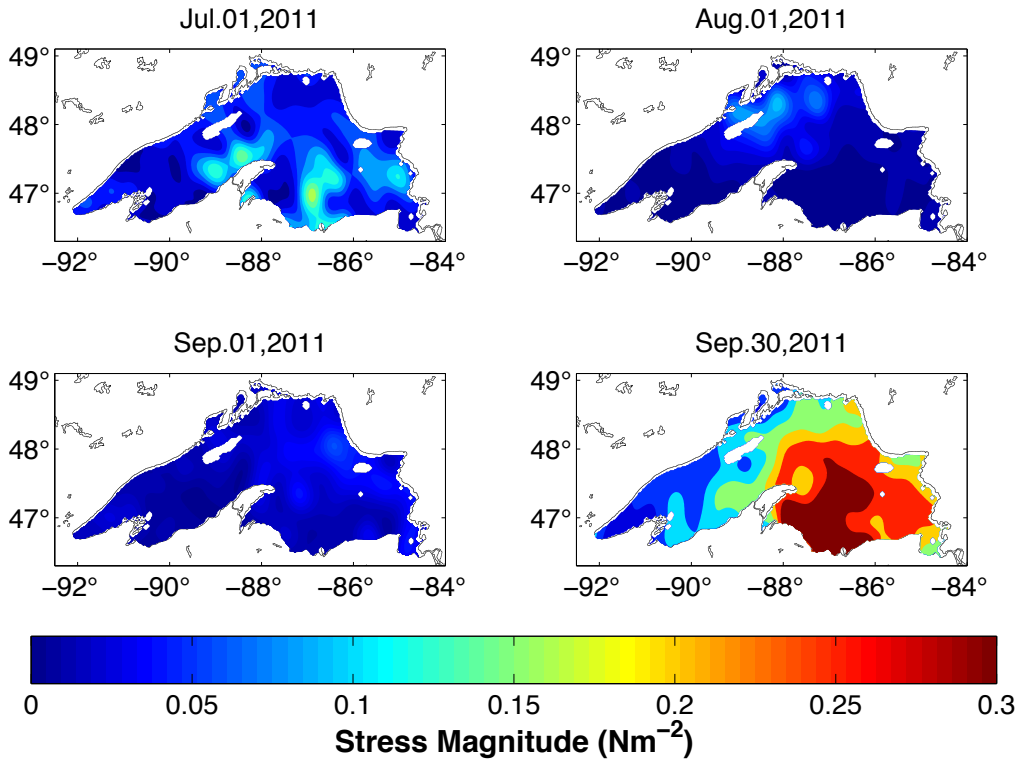

Figure 3.3: **NARR Stress.** Snapshots of spatially / temporally varying wind stress magnitude derived from NARR climatology output.

The modeled wind stress, derived from NARR wind speeds, was compared to observed wind stress, derived from National Data Buoy Center (NDBC) buoy wind speeds. The magnitude and direction of the NARR wind stress is consistent with NDBC wind stress (Figure 3.4 - 3.5). The correlation between the observed and modeled wind stress at the core mooring sites is provided in Table (3.2).

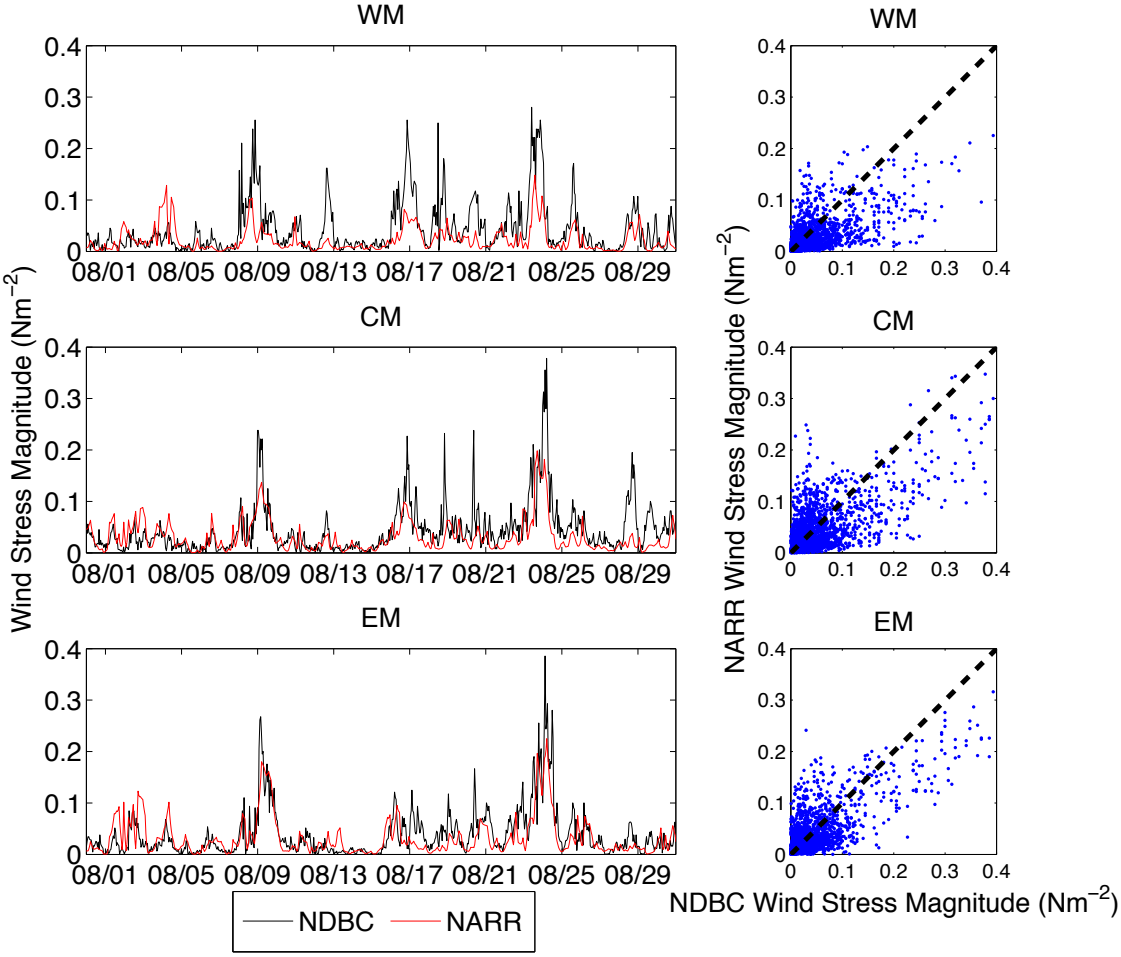

Figure 3.4: **NDBC Stress Magnitude vs NARR Stress Magnitude.** Thirty day comparison between the magnitude of observed wind stress at the core mooring sites, computed using NDBC data, to the magnitude of wind stress computed from NARR wind field. The black line represent the observed (NDBC) data and the red line represent the NARR data. The second column shows a cross plot of the magnitude of NARR wind stress and magnitude of NDBC wind stress at each mooring site. The cross plots include all 92 days of output.

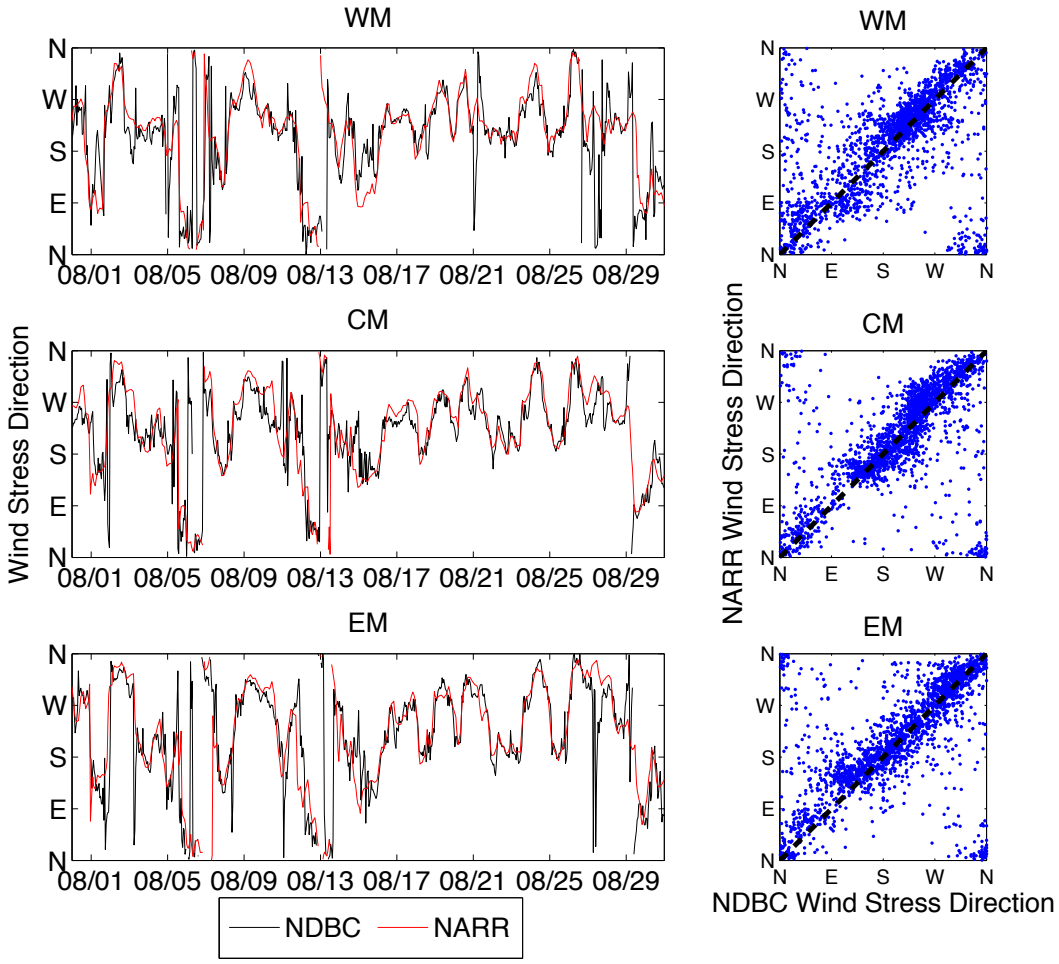

Figure 3.5: **NDBC Stress Direction vs NARR Stress Direction.** Thirty day comparison between the direction of observed wind stress at the core mooring sites, computed using NDBC data, to the direction of wind stress computed from NARR wind field. The black line represent the observed (NDBC) data and the red line represent the NARR stress. The second column shows a cross plot of the direction of NARR wind stress and direction of NDBC wind stress at each mooring site. The cross plots include all 92 days of output.

Table 3.2: NARR Stress Magnitude / NDBC Stress Magnitude Correlation

Mooring Name	Correlation Stress Magnitude
Western Mooring (WM)	0.66
Central Mooring (CM)	0.77
Eastern Mooring (EM)	0.86

3.1.4 Computation

Computation was done at the Minnesota Supercomputing Institute (MSI) located on the Twin Cities campus of the University of Minnesota. The model domain was partitioned into 16 equal pieces each computed on different computing nodes on MSI's Calhoun cluster. Calhoun is an SGI Altix XE 1300 Linux cluster with 180 SGI Altix XE 300 computing nodes. Each node contains two quad-core 2.66 GHz Intel Xeon processors sharing 16 GB of memory. In total, Calhoun consists of 1440 computing cores and 2.8 TiB[1] of main memory. A simulation lasting 90 days and outputting every hour took approximately 16 hours to complete using 16 processors.

3.2 Observations

3.2.1 Lake Superior Mooring Array

The Lake Superior mooring array is a collection of up to seven moorings which have been continuously deployed starting in 2005 (Figure 3.6). In 2005 the Western Mooring (WM) was deployed and was the only mooring for three years. The Eastern (EM) and Central (CM) Moorings were included in the array in 2008 to increase spatial coverage. These three moorings form the "core mooring" array, which is still in operation today. The core moorings locations were chosen to be within 1 km to 2 km of NDBC buoys. with the WM, CM, and EM locations coinciding with NDBC buoys 45006, 45001, and 45004, respectively. Supplemental moorings have been included in the array to increase spatial coverage. These include the Far Western (FWM); Northern (NM); Southern

[1] 1 tebibyte (TiB) = 1024 gigabytes (GB)

(SM); and Far Eastern Moorings (FEM). However, these supplemental moorings were only in operation from 2008 to 2012. The moorings remain in continuous operation once deployed, apart from a brief removal once or twice a year to replace batteries and retrieve data. Table (3.3) gives the location and depth of each mooring. Instruments on the mooring lines have included thermistor strings, Acoustic Doppler Current Profilers (ADCP), ice profilers, O_2 sensors, NO_3 sensors, and sedime traps. However, this thesis will only discuss thermistor and ADCP data sets.

Each mooring is equipped with 10 to 13 thermistors irregularly spaced throughout the water column. Thermistors are spaced closer together near the surface to capture the sharp temperature change in the thermocline during the stratified season and coarsely spaced near the bottom where the temperature remains relatively constant throughout the year. Due to coast guard restrictions, instruments had to be at least 10 m below the surface. The coincident NDBC buoy can be used to fill in the temperature gap near the surface, since they record temperature at 1 m depth. The anchor and acoustic release limit the bottom thermistor to a depth of 5 meters above the lake bed.

A few different thermistor models have been included on the moorings, including Brancker Research (RBR) TR-1000, TR-1050, TR-1060, and TD-2050 sensors, and Seabird Electronics SBE-39 and SBE-39P sensors. Pressure sensors are deployed at 10 m and 100 m to validate the sensor position on the mooring line. The storage capacity of each instrument limits the sampling rate, with the TR-1000 and SBE sensors taking measurements every 10 minutes, and the TR-1050, TR-1060, and TD-2050 sensors taking one measurement every minute.

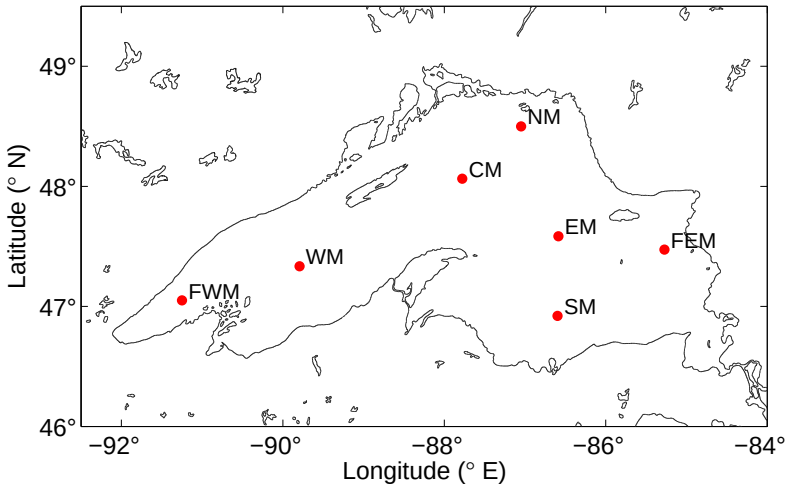

Figure 3.6: **Lake Superior Mooring Array.** Locations of active and inactive moorings in Lake Superior deployed since 2005

Table 3.3: Mooring Array

Mooring Name	Latitude	Longitude	Depth (m)
Western Mooring (WM)	47° 19.018’	89° 48.520’	185
Central Mooring (CM)	48° 1.384’	87° 46.006’	255
Eastern Mooring (EM)	47° 32.186’	86° 34.261’	213
Far Western Mooring (FWM)	47° 3.005’	91° 14.928’	170
Northern Mooring (NM)	48° 29.972’	87° 2.935’	201
Southern Mooring (SM)	46° 55.252’	86° 35.805’	384
Far Eastern Mooring (FEM)	47° 28.375’	85° 16.394’	247

3.2.2 Acoustic Doppler Current Profilers

An ADCP sends out a pulse of sound at a specific frequency which reflects off passively moving particles in the water. The range of the moving particle can be calculated by $R = \frac{1}{2}tc$, where t is the round trip time of the signal and c is the speed of sound in

water (c $\approx$ 1500 ms^{-1}) (Bugnon and Whitehouse 1991). The frequency of the return signal will be Doppler shifted and yield information about the velocity of the moving particle, $f_d = \frac{2v}{c} f_o$, where f_d is the Doppler shift in the original frequency, f_o, and v is the velocity of the moving particle. The ADCP's transducers are arranged in a Janus configuration [2] , which allows the velocity vector to be broken down into zonal (east-west component), meridional (north-south component), and vertical components. ADCPs have been routinely placed with the core moorings and have been sporadically included in the FWM and NM. ADCPs are placed 80 m below the surface and faced upward making readings every 2 meters. Spurious reflections can occur from fish or other instruments on the mooring line. The deployment history of ADCPs at each mooring site is shown in Figure 3.7.

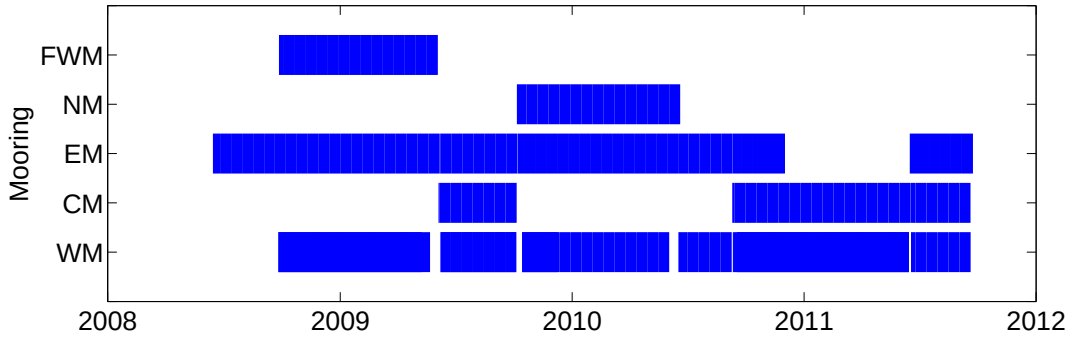

Figure 3.7: **ADCP Deployment Record.** Deployments of upward or downward looking ADCPs at mooring sites.

3.3 Mathematical Methods

3.3.1 Wavelet Analysis

Many geophysical time series have non-stationary statistics, i.e. the mean and variance change with time. A Fourier transform can be used to determine whether a frequency is present in a time series, however, a periodogram of the Fourier transform does not give any information about how the amplitude of each frequency varies with time. A simple way to deal with non-stationary time series is to compute a running variance and running

[2] Janus is the roman god of beginnings depicted with two faces looking in opposite directions.

mean, however, this contains no frequency information and is highly dependent on the length of the window and type of window used. To gain information about the frequency of a periodic signal a running Fourier transform can be used. This involves sliding a window over a time series and computing the fast Fourier transform (FFT) at each time (using only the data inside the window). The running Fourier transform poorly resolves high and low frequencies since the window width limits the frequencies that can be resolved. Wavelet analysis attempts to solve this time and frequency localization problem.

Wavelet analysis is used to study the temporal variability of power at many different frequencies. A wavelet is a function which has zero mean and is localized in time and frequency space. Traditionally, wavelets from a spectrum of frequencies are convoluted with a time series. This thesis will only use wavelets tuned to a specific frequency, e.g. the inertial frequency. Time series were convoluted using a clockwise and counter-clockwise rotating Morlet wavelet of the form:

$$w_{\pm}(t_0) = (\tau\sqrt{\pi})^{-1} e^{-(\frac{(t-t_0)}{\tau})^2} e^{\mp i\omega t} \tag{3.6}$$

where τ is window width, ω is the frequency of the wavelet, t is time vector, and t_0 is the central position in time of the wavelet. Power is determined using

$$P_{\pm}(t) = \int_{-\infty}^{\infty} w_{\pm} U \, \mathrm{d}t \tag{3.7}$$

where $U = u + iv$ is the complex velocity (u is the zonal component while v is the meridional component). The power yields information about the magnitude and phase of the NIWs. The real and imaginary components of the complex Morlet wavelet are formed from the product of a Gaussian curve and a sinusoid (Figure 3.8).

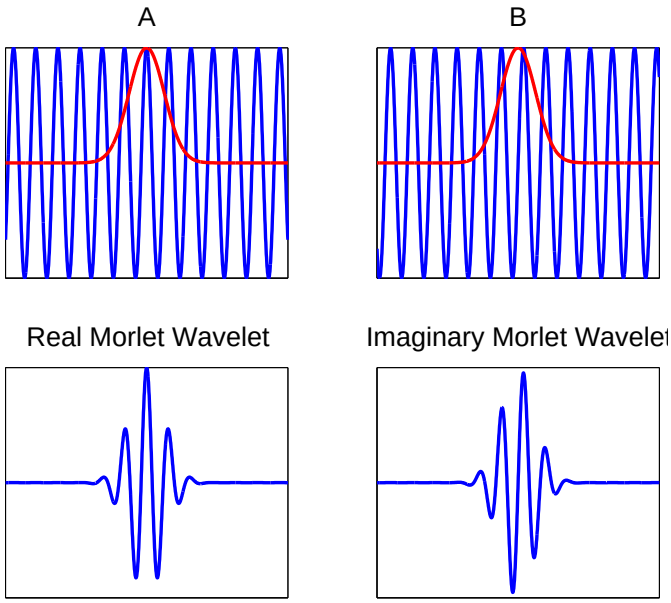

Figure 3.8: **Complex Morlet Wavelet.** Column A shows the product of a Gaussian curve and a cosine function while column B shows the product of a Gaussian curve and a sine function. The bottom row shows the result of these products, which are the real and imaginary component of the Morlet wavelet.

3.3.2 Near-Inertial Potential Energy

The vertical stratification scale, which is a measure for the depth of the thermocline, was estimated by the following equation [3] :

$$z_s = \frac{\sum_{i=1}^{N} \frac{\Delta T_i}{\Delta z_i} z_{i,mid}}{\sum_{i=1}^{N} \frac{\Delta T_i}{\Delta z_i}} \tag{3.8}$$

where N is the number of thermistors, z_{mid} is the mid point between adjacent grid cell, ΔT_i is the temperature difference of the adjacent grid cells, and Δz_i is the distance between each vertical grid cell.

[3] Another method to estimate the vertical stratification scale for discrete data can be found in Austin and Allen (2011). The vertical stratification scale for continuous data can be estimated by the maximum Brunt-Väisälä frequency.

Potential energy can be calculated by the following equation :

$$PE = \rho g \eta_2 \tag{3.9}$$

where PE is the potential energy per unit volume, ρ is the density of water, g is the gravitational acceleration, and η_2 is the amplitude of the internal interface [4] . η_2 can be calculated by the following expression :

$$\eta_2 = z_s - z_s^* \tag{3.10}$$

where z_s is the thermal stratification scale, and z_s^* is the low pass filtered thermal stratification scale. The potential energy can be estimated by η_2, if ρ and g can be assumed constant.

3.3.3 Near-Inertial Kinetic Energy

Near-inertial kinetic energy is carried by currents in the water column. Since Lake Superior is a large Burger number lake most of the NIW energy is carried in kinetic energy (Antenucci and Imberger 2001).

The classical expression for kinetic energy can be used to estimate the kinetic energy of a fluid column :

$$KE = \sum \frac{1}{2} v_i^2 \Delta m_i \tag{3.11}$$

$$= \frac{1}{2} \sum \rho_i A v_i^2 \Delta z_i \tag{3.12}$$

Where m_i is the mass of each parcel of fluid, v_i is the magnitude of the velocity at each depth i, A is the surface area of each parcel, and Δz_i is the thickness of each layer. If the surface area of each parcel is a constant then we can write the kinetic energy per area :

$$\frac{KE}{A} = \frac{1}{2} \sum \rho_i v_i^2 \Delta z_i \tag{3.13}$$

Given raw velocity magnitudes this expression will not tell us anything about energy at the inertial frequency. In order to estimate kinetic energy associated with the inertial

[4] See Figure 2.2 for a visual representation of η_2.

frequency a measure for the inertial velocity needs to be established. Wavelet analysis and the rotary spectrum can be used to isolate the inertial velocity. The amplitude of the wavelet power can be used as an estimator of the magnitude of the inertial velocity (if the wavelet used is tuned to the inertial frequency). This method has the advantage of looking at temporal variations in the magnitude of inertial velocity, and hence inertial energy. Another method is to integrate under the inertial band of frequencies in a rotary spectrum and then take the square root of the result. This method takes into account the entire time series and therefore temporal information is lost, but this method has the advantage of defining one number for the inertial velocity. To speed up computation time, it was assumed the inertial energy at the surface is representative of the total integrated kinetic energy. This can be justified since the total response is proportional to the surface response. The kinetic energy will also be weighted by the water depth at each point to take into account bathymetric effects. The expression below was used to estimate near-inertial kinetic energy per unit volume :

$$\frac{KE}{V} = \frac{\frac{1}{2}\rho_{surf} v_{inertial}^2 \Delta z_{surf}}{H} \tag{3.14}$$

Where ρ_{surf} is the water density at the surface, $v_{inertial}$ is the magnitude of the inertial velocity estimated from the amplitude of the clockwise wavelet power at inertial frequency, Δz_{surf} is the depth at which the velocity measurement was taken, H is the depth of the water column, and $\frac{KE}{V}$ is the kinetic energy per unit volume, where $V = AH$.

Chapter 4

Results

4.1 Rectangular Basin Simulations

Flat bottom rectangular basins were used to explore the effect of top-hat wind stresses with various durations and thermal structures on the distribution of near-inertial energy. The flat bottom 200 km by 200 km closed boundary basin with a two layer thermal structure produced substantial internal waves under top-hat wind forcing. The flat bottom 200 km by 200 km closed boundary basin with uniform temperature distribution produced weak inertial waves. The flat bottom basin with periodic boundaries and a two layer thermal structure produced pure inertial oscillations, but no displacement of the thermocline.

4.1.1 Ideal Basin : Closed Boundaries, two-layer

The ideal basin was 200 km by 200 km with a uniform depth of 165 m. The model was forced with a spatially uniform top-hat wind stress with a magnitude of 0.1 Nm^{-2} directed to the east, the direction does not affect the dynamics of the water column. The thermal structure for the two layer system had the thermocline depth set to 20 m. The temperature of the surface mixed layer was $21°C$, and the temperature of stagnant bottom layer was $4°C$. These values are representative of Lake Superior summer conditions.

The temperature at the central point in the ideal basin shows that the thermocline starts to oscillate after an internal wave has propagated 100 km (Figure 4.1), suggesting

that a divergence in the flow is necessary to start pumping the thermocline. Undulations of the thermocline are initiated at convergence zones where upwelling or downwelling occurs. The time it takes this wave to reach the center of the basin is given by dividing the distance from shore by the internal wave speed ($t = \frac{d}{c_{int}}$).

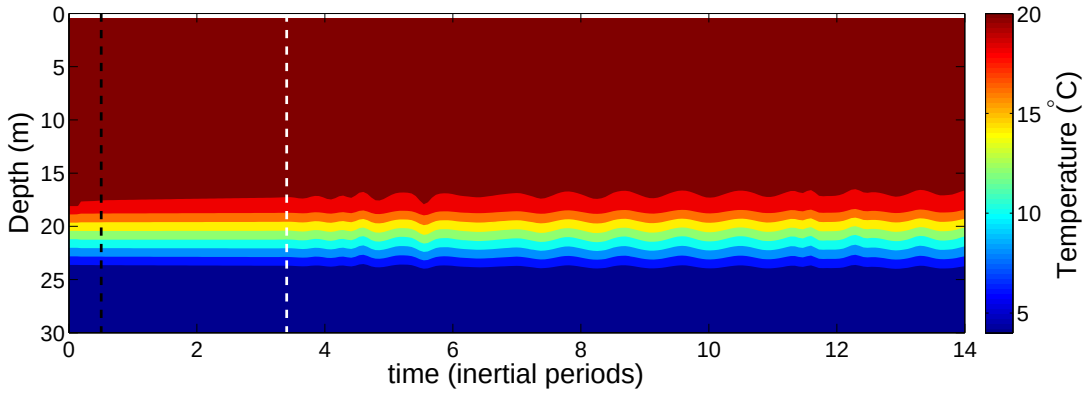

Figure 4.1: **Temperature - Ideal Basin (Closed Boundaries).** Temperature profile at the center of the ideal basin for the top 30 m of the water column. The black dotted line is the end of forcing. The white dotted line is the time it takes an internal wave to propagate 100km. The x-axis is in units of inertial periods, where the inertial period is about 16 hours.

Higher velocity magnitudes were observed in the upper layer compared to the lower layer and periodic velocity components were observed throughout the water column (Figure 4.2). The velocity at the surface contains a significant amount of clockwise energy near the inertial frequency (Figure 4.4). At each depth the velocity vector is rotating clockwise, with higher velocity magnitudes in the upper mixed layer (Figure 4.3). This is indicative of inertial waves in the northern hemisphere. The evolution of surface inertial energy is shown in (Figure 4.5). The energy is weakest at the coast and after about 11 inertial periods most of the energy stays concentrated near the center of the basin.

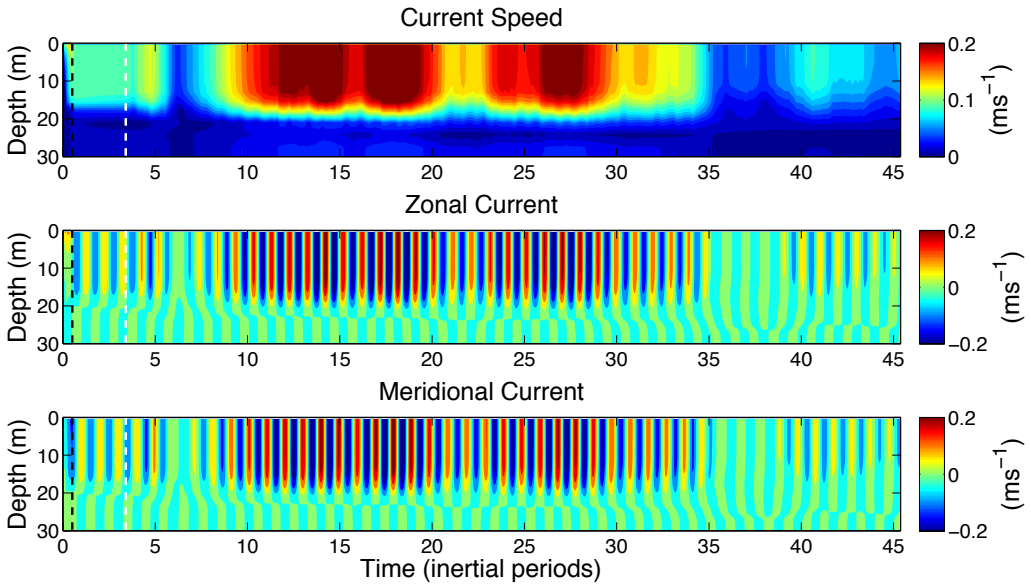

Figure 4.2: **Velocity Profile - Ideal Basin (Closed Boundaries).** Velocity profile at the center of the ideal basin for the top 30 m. The black dotted line is the duration of the forcing. The white dotted line is the time it takes an internal wave to propagate 100 km The x-axis is in units of inertial periods, where the inertial period is about 16 hours.

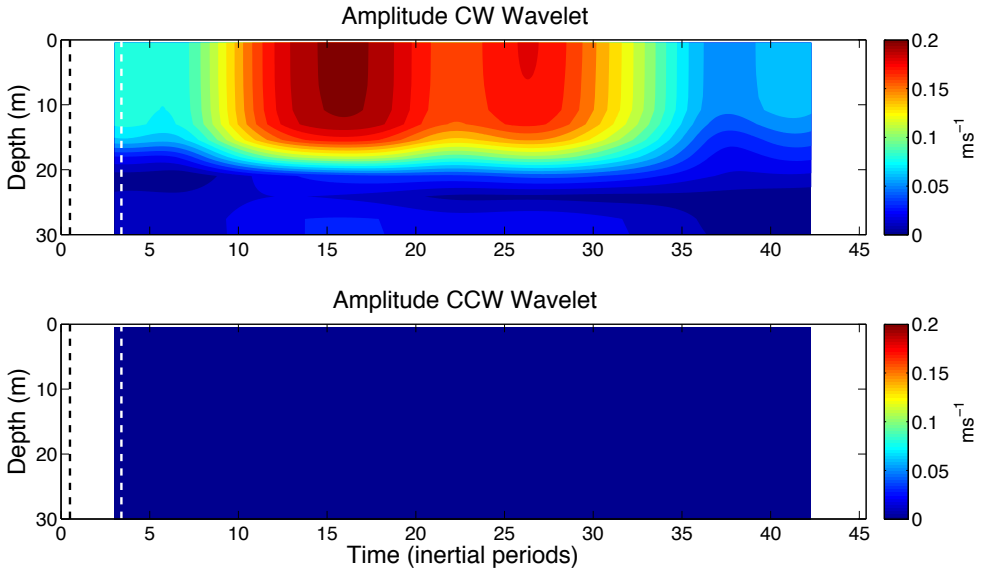

Figure 4.3: **Wavelet Amplitude - Ideal Basin (Closed Boundaries).** Vertical profile of the amplitude of the clockwise wavelet power at the center of the ideal basin. The black dotted line is the duration of the forcing. The white dotted line is the time it takes an internal wave to propagate 100 km. The x-axis is in units of inertial periods, where the inertial period is about 16 hours.

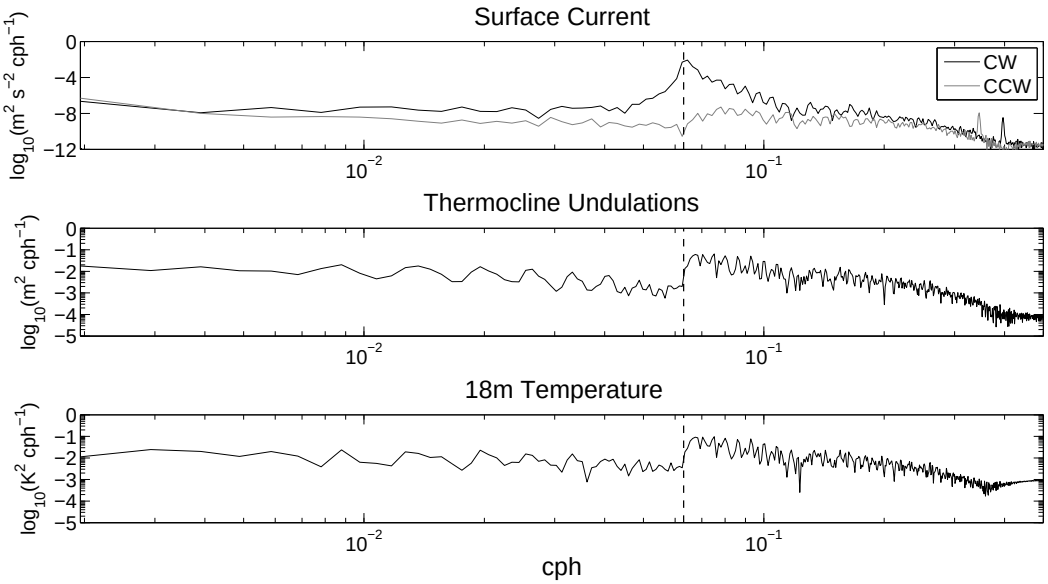

Figure 4.4: **Spectra - Ideal Basin (Closed Boundaries).** Spectra from surface velocity, thermocline undulations, and 18 m temperature. The black dotted line is at the inertial frequency.

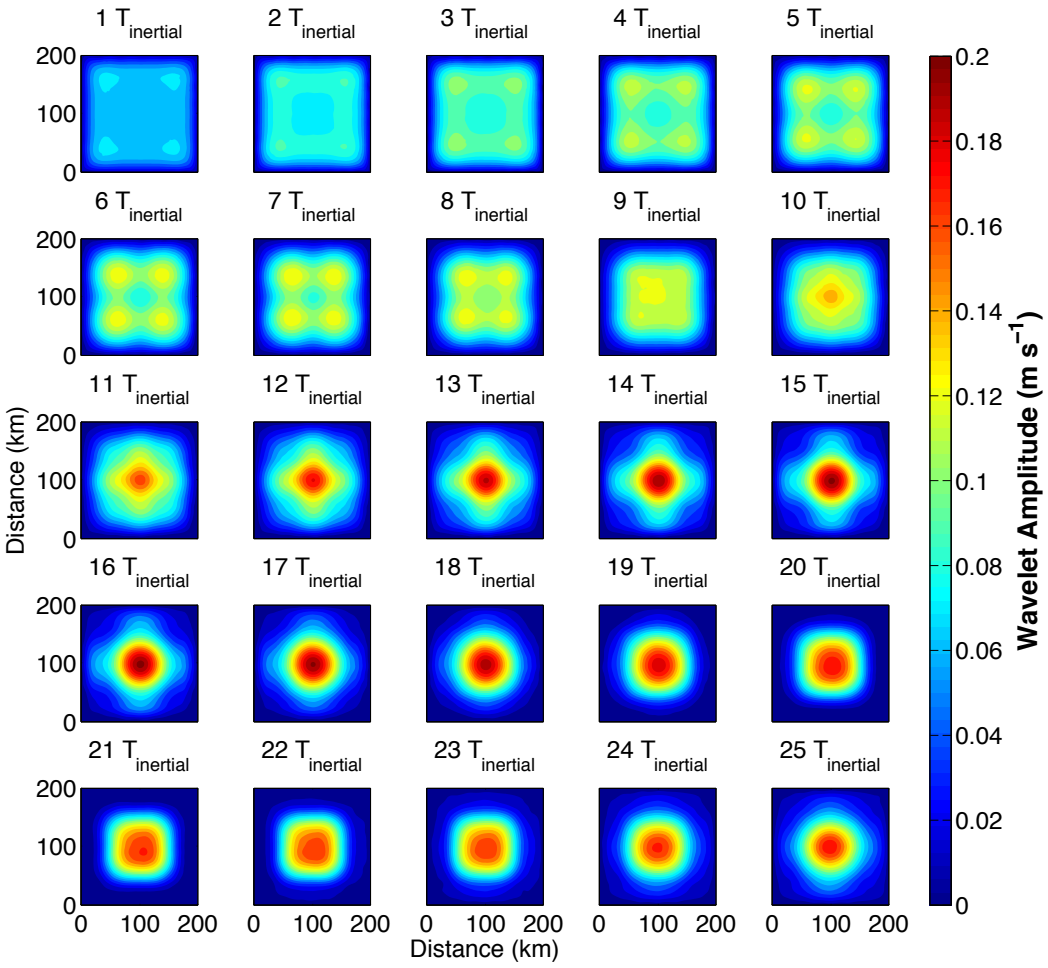

Figure 4.5: **Surface Inertial Energy - Ideal Basin (Closed Boundaries).** Spatial distribution of the amplitude of the wavelet power. The time between each snapshot is one inertial period ($T_{inertial} = 16$ hours).

4.1.2 Ideal Basin : Isothermal

An identical ideal basin, 200 km by 200 km, with a uniform depth of 165 m was used with uniform thermal structure. The model was forced with a spatially uniform top-hat wind stress with a magnitude of 0.1 Nm^{-2} directed to the east, the direction does not affect the dynamics of the water column. The thermal structure was a uniform $4°C$.

Weak inertial energy was observed in the simulation. The components of the velocity

at the center of the basin shows weak inertial motion in the top 30 m (Figure 4.6). Also, a small amount of clockwise energy at the inertial frequency was observed in the spectrum of velocity at center of the basin (Figure 4.7).

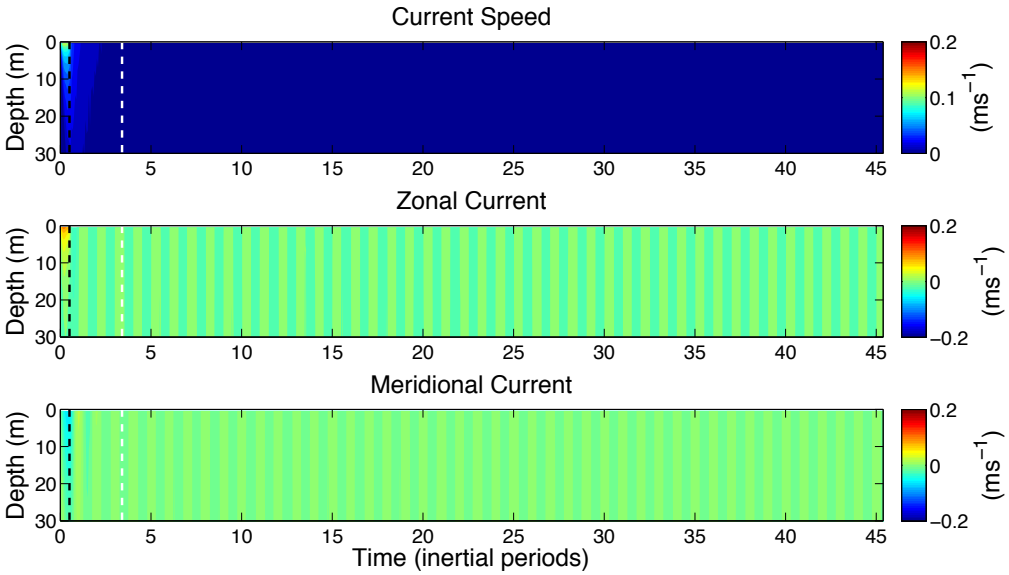

Figure 4.6: **Velocity Profile - Ideal basin (Isothermal).** Velocity profile at the center of the ideal basin for the top 30 m. The black dotted line is the end of the forcing. The white dotted line is the time it takes an internal wave to propagate 100 km. The x-axis is in units of inertial periods, where the inertial period is about 16 hours.

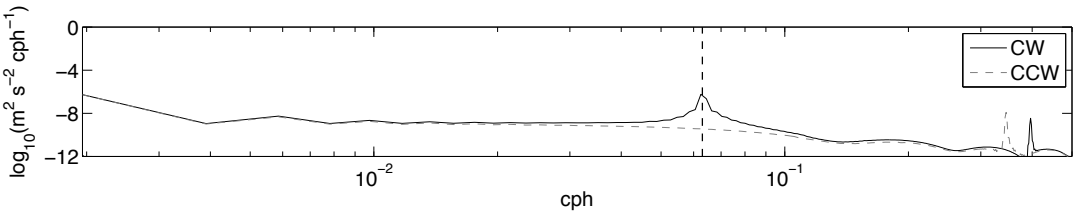

Figure 4.7: **Spectra - Ideal Basin (Isothermal).** Spectra from surface velocity at a center of an ideal basin with a uniform thermal structure of $4°C$. The black dotted line is at the inertial frequency.

4.1.3 Ideal Basin : Periodic Boundaries

A model with doubly periodic boundary conditions was used to show that a divergence in the flow, such as flow perpendicular to a coast, is necessary for undulations of the thermocline to begin. No oscillations of the thermocline were observed in the simulation with periodic boundaries (Figure 4.8). The meridional and zonal components of the velocity in the mixed layer are periodic (Figure 4.9). Also, high velocity magnitudes were observed in the top layer and no motion in the bottom layer, any apparent motion below the thermocline is due to ambient noise. The periodic component of the velocity in the top layer shows pure inertial motion (Figure 4.10).

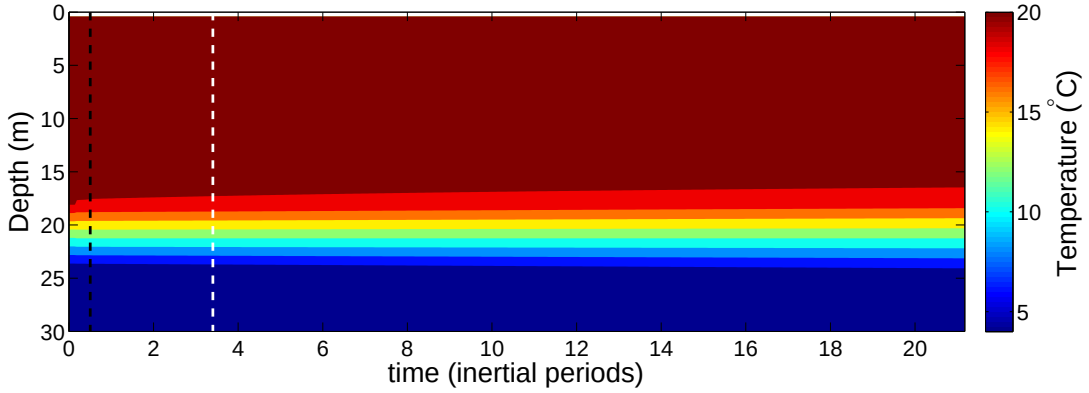

Figure 4.8: **Temperature - Ideal Basin (Periodic Boundaries).** Temperature profile at the center of the ideal basin with periodic boundaries for the top 30 m. The black dotted line is the end of the forcing. The white dotted line is the time it takes an internal wave to propagate 100 km. The x-axis is in units of inertial periods, where the inertial period is about 16 hours.

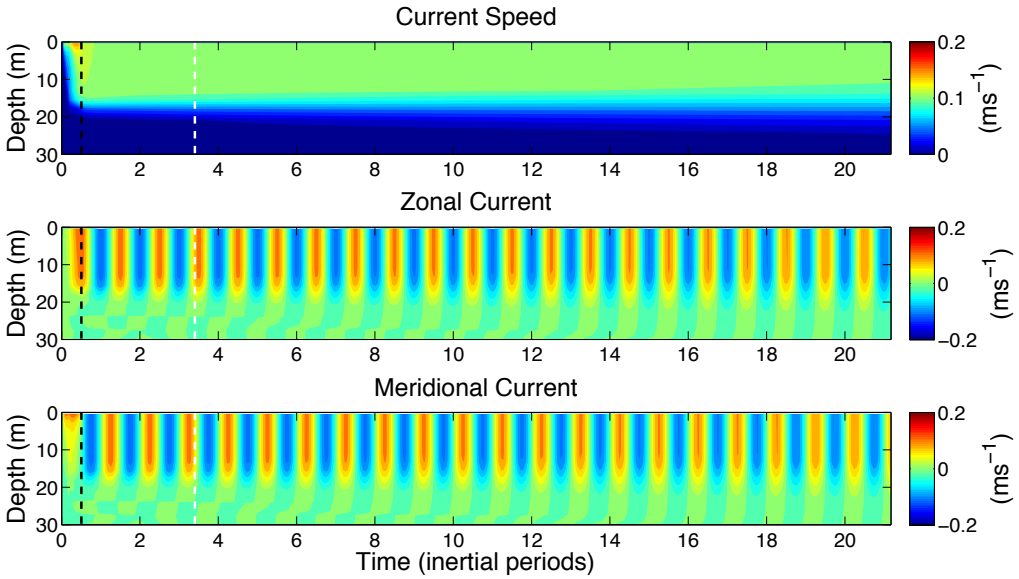

Figure 4.9: **Velocity Profile - Ideal Basin (Periodic Boundaries).** Velocity profile at center of ideal basin with periodic boundaries for the top 30 m. The black dotted line is the end of the forcing. The white dotted line is the time it takes an internal wave to propagate 100 km. The x-axis is in units of inertial periods, where the inertial period is about 16 hours.

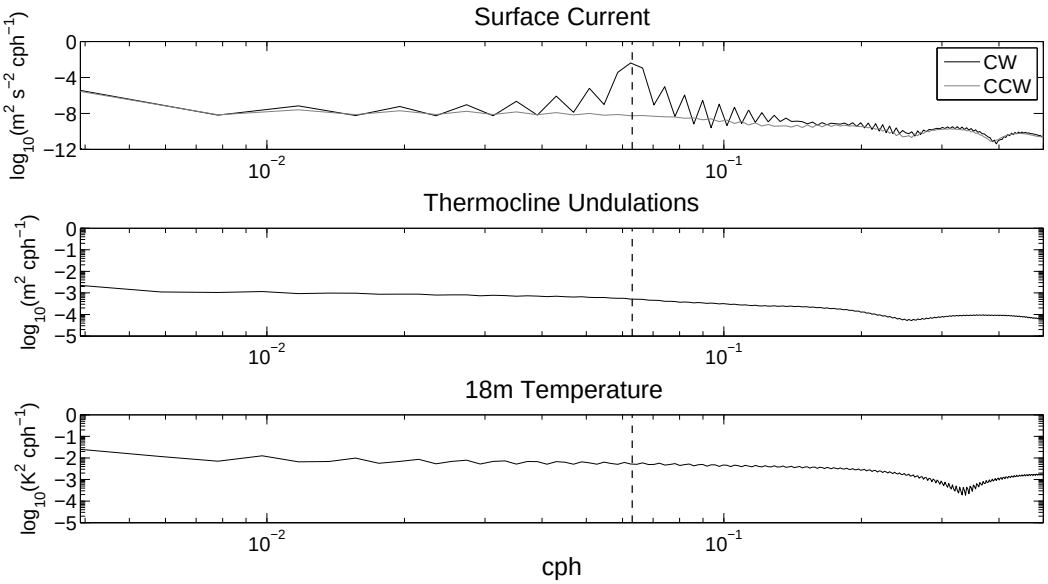

Figure 4.10: **Spectra- Ideal Basin (Periodic Boundaries).** Spectra from surface velocities, thermocline undulations, and 18 m temperature. The black dotted line is at the inertial frequency.

4.2 Lake Superior Basin Simulations

Two types of Lake Superior basins were explored. First, a flat bottom basin with Lake Superior coastline was used to explore the bulk response of the lake. Then, realistic bathymetry was included to explore the effects of bathymetry on the spatial distribution of near-inertial energy. The realistic bathymetry simulation was compared with observational data from the core mooring sites.

4.2.1 Lake Superior : Flat Bottom

The flat bottom Lake Superior simulation was configured using 2 km x 2 km spatial resolution and a uniform depth of 165 m with two layer thermal structure and uniform wind stress. The forcing used was a top-hat wind stress lasting for half an inertial period. To estimate the inertial energy across the basin a rotary spectrum was applied to the surface velocities and the peak in the clockwise rotary spectrum at the inertial

frequency was used as an estimate for the inertial energy. The inertial energy is large away form shore and weakest close to shore (Figure 4.11).

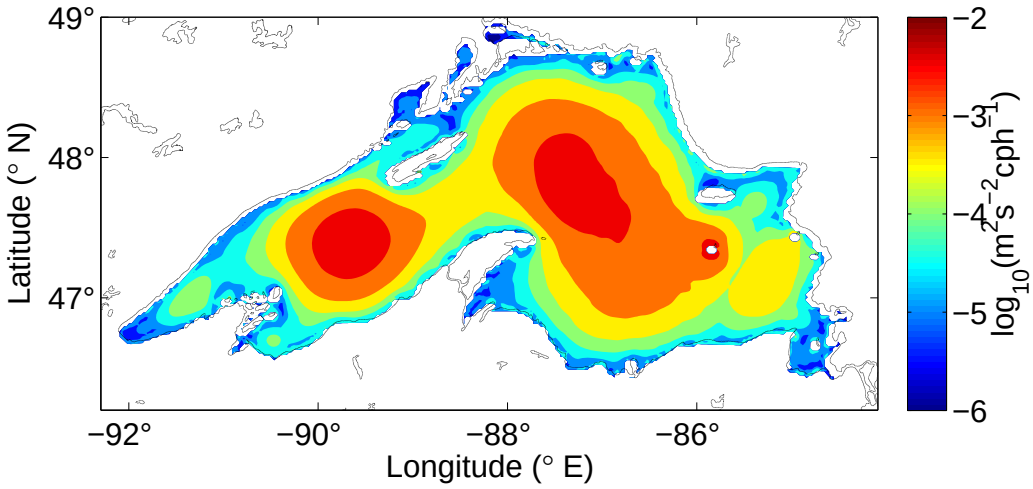

Figure 4.11: **Surface Inertial Energy - Lake Superior (Flat Bottom).** Peak in the clockwise rotary spectrum at the inertial frequency.

4.2.2 Lake Superior : Realistic Bathymetry

The realistic bathymetry Lake Superior simulation used a 2 km by 2 km closed basin forced with realistic wind stress derived from the 2011 NARR wind field. Stations were placed in the model co-located with the core mooring sites. To validate the model the nodal points of the first three seiche modes were compared with nodal points calculated by Rao and Schwab (1976), who used a numerical procedure to calculate seiche modes in a 5 km by 5 km Lake Superior basin with realistic bathymetry. The nodal points in the primate equation model (ROMS) corroborate the work by Rao and Schwab (1976) (Figure 4.12).

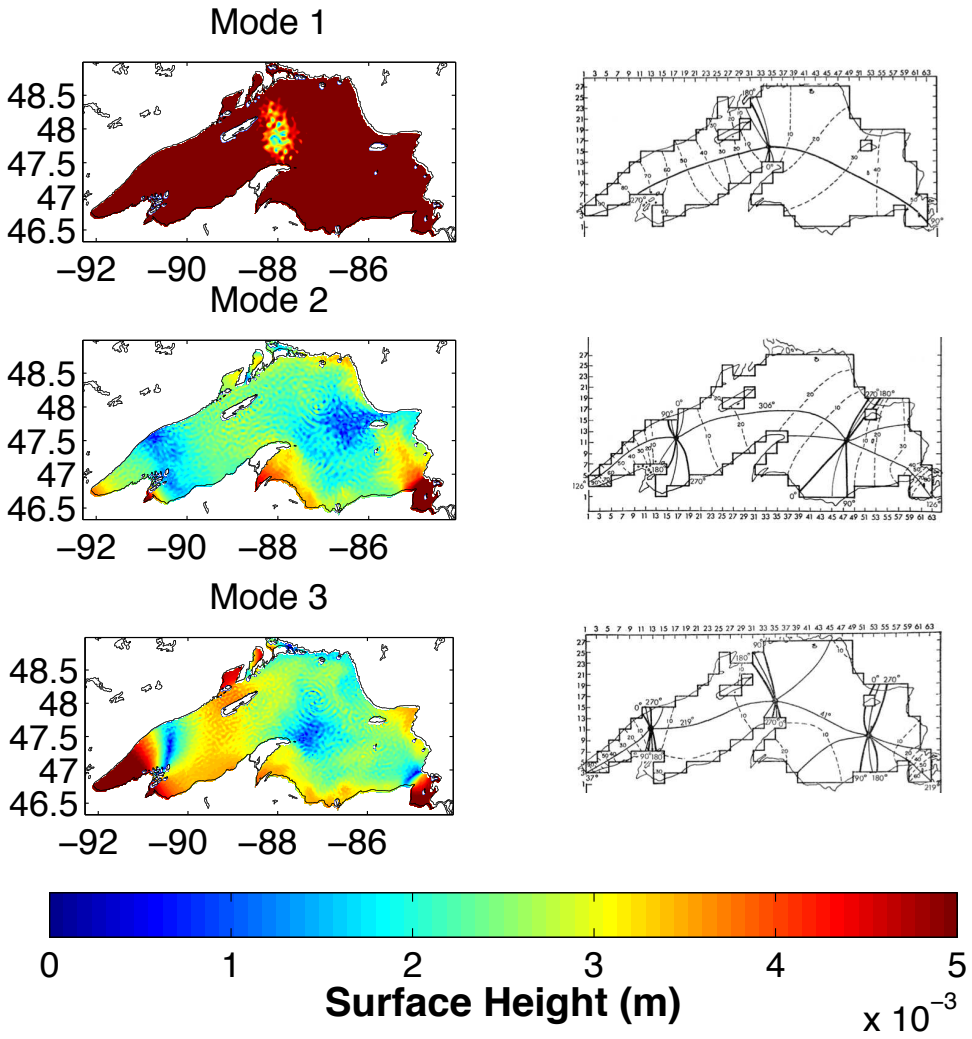

Figure 4.12: **Seiche Modes.** Nodal points for the first three seiche frequencies. The first column shows surface height for the first three seiche periods estimated using a primitive equations model. The second column shows the nodal points calculated using a numerical procedure (Rao and Schwab 1976)

Two methods were used to estimate the surface inertial energy in model results. The amplitude at the inertial frequency of the clockwise rotary spectrum was used to estimate the average kinetic energy (Figure 4.13). The volume averaged inertial kinetic energy shows enhanced energy around shallow points in the model (Figure 4.14). The

amplitude of the clockwise wavelet power was used as an estimate of inertial velocities to look at the temporal evolution of surface kinetic energy (Figure 4.15)

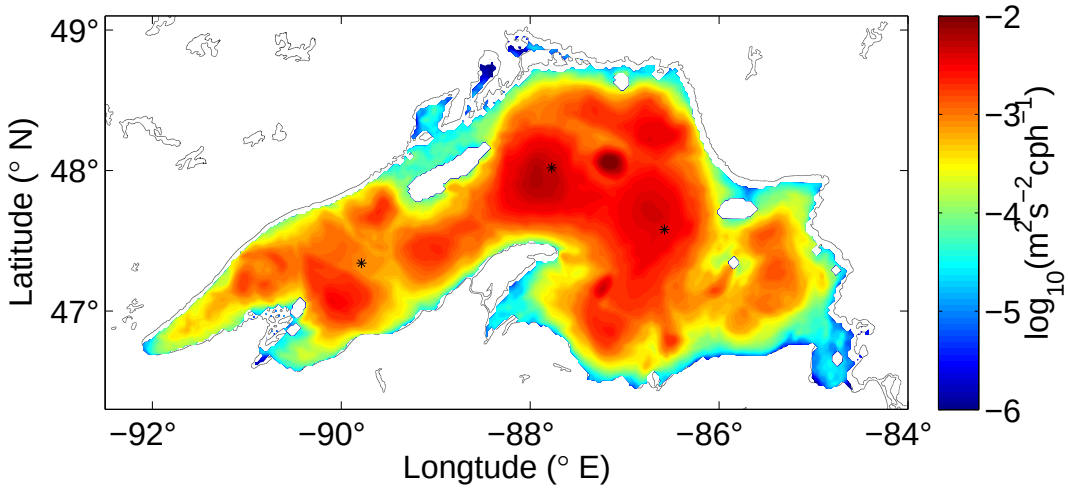

Figure 4.13: **Surface Inertial Energy - Lake Superior (Realistic Bathymetry).** Peak in the clockwise rotary spectrum at the inertial frequency.

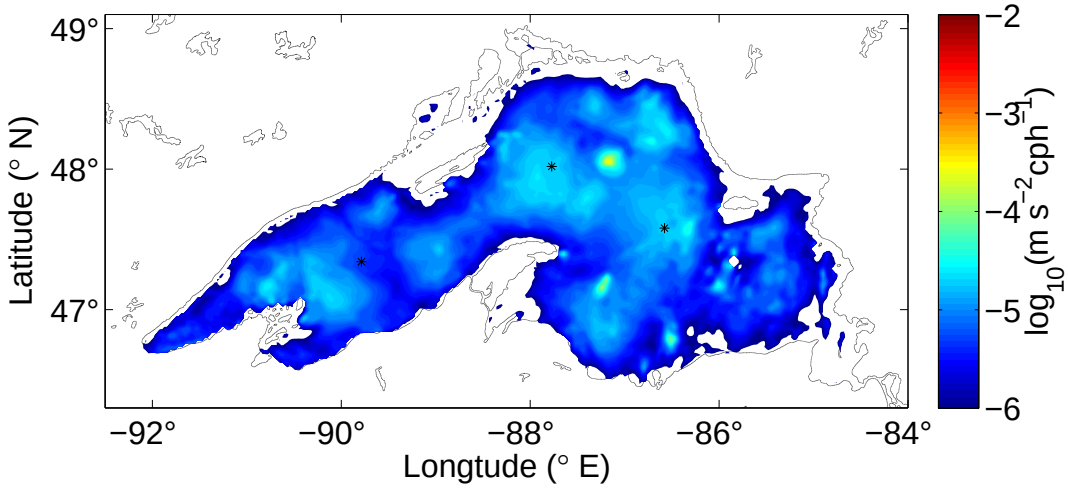

Figure 4.14: **Surface Inertial Energy per Volume - Lake Superior (Realistic Bathymetry).** Peak in the clockwise rotary spectrum at the inertial frequency weighted by depth at each point.

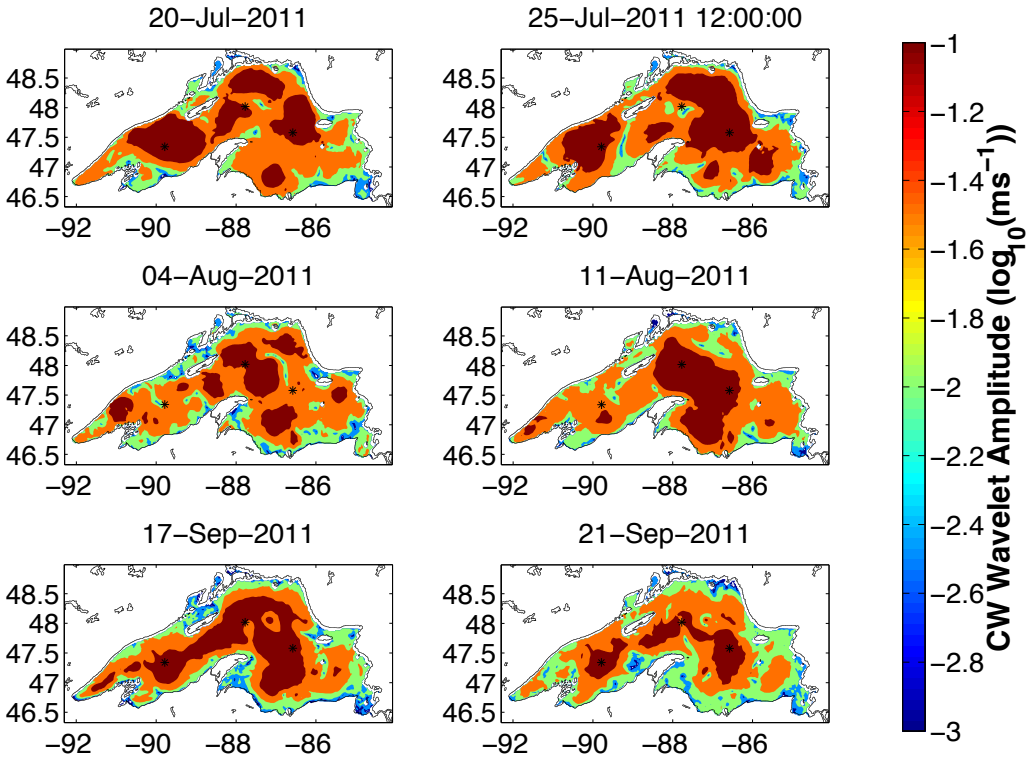

Figure 4.15: **Wavelet Amplitude - Lake Superior (Realistic Bathymetry).** Surface kinetic energy distribution computed using the amplitude of clockwise rotary wavelet tuned to the inertial frequency. The black dots represent the core mooring sites. Each row represents a local inertial event. The column on the left is before the event and the column on the right is after the event.

Austin (2013) described a method to calculate the wavelength and wave direction of inertial waves based on the theory of a propagating plane wave in a two layer system. In model results, the direction of propagation of inertial waves at the core mooring sites veers counter-clockwise with a period of about 30 days (Figure 4.16). Austin (2013) observed a similar result in Lake Superior. Austin (2013) also observed the horizontal wavelength of NIWs to be 30 km - 60 km, smaller than what is predicted by ROMS [1] .

[1] Appendix C explains the method to calculate the wavelength of NIWs, which was presented in Austin (2013).

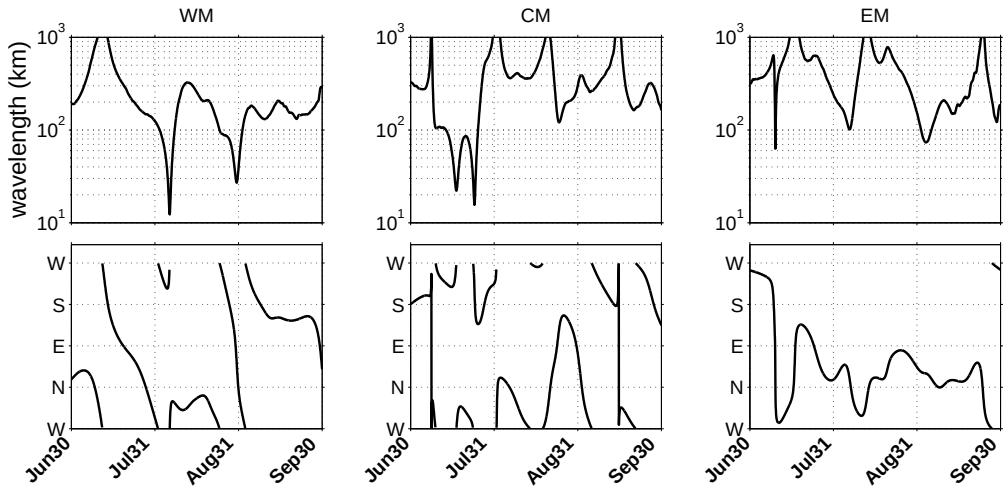

Figure 4.16: **Wave Climate - Lake Superior (Realistic Bathymetry).** Estimated wavelength and direction of wave propagation at core mooring sites in the model. The top is the estimated wavelength and the bottom row is the direction of wave propagation.

The phase difference of the clockwise rotary wavelet tuned to the inertial frequency between two sites yields information about the phase of inertial waves. This method was applied to the core sites and reveals that the phase of the inertial wave between sites varies between -2π and 2π (Figure 4.17). Since the phase of the inertial wave is not phase locked suggests that the spatial structure of near-inertial waves does not have a simple modal structure.

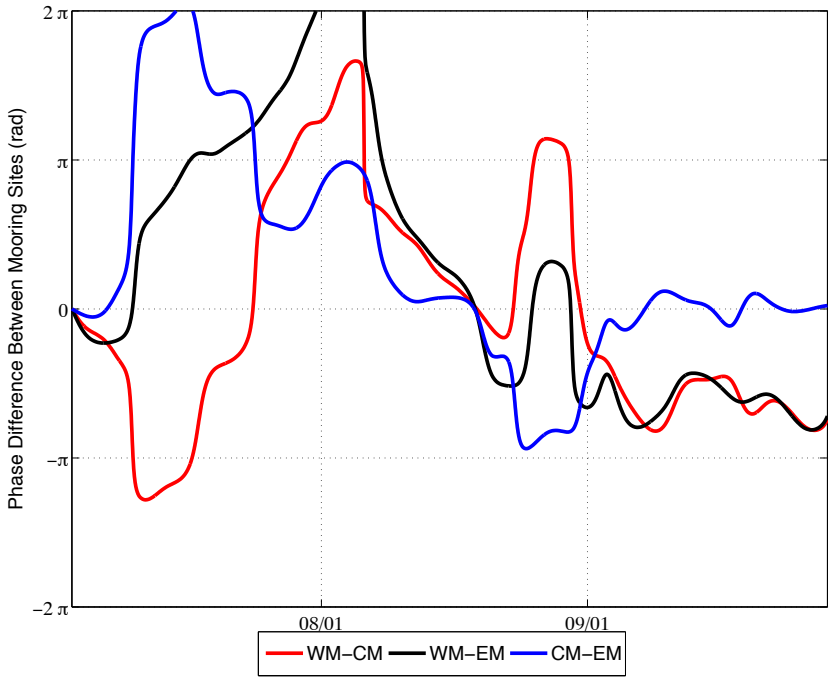

Figure 4.17: **Modeled Near-inertial Phase - Core Mooring Sites.** Phase difference between core mooring sites during the study period.

The magnitude of the velocity at the bottom grid cell is greater than 0.10 ms^{-1} close to shore and over the Keweenaw ridge (Figure 4.18). These large magnitudes have the potential to resuspend sediment.

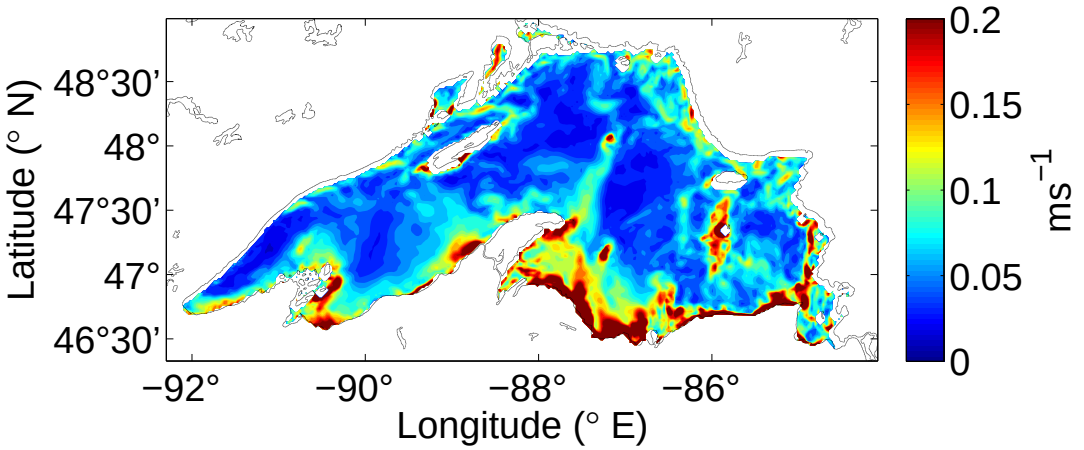

Figure 4.18: **Maximum near bottom velocity magnitude.** Maximum magnitude of velocity in bottom grid cell during the study period.

4.3 Observations

Inertial energy is present in vertical velocity profiles and thermocline undulations, but is not significant in water level records (Figure 4.19). However, a spectrum of the water level record does show a broad peak at the seiche frequencies, and even more interesting, sharp peaks at the tidal frequencies.

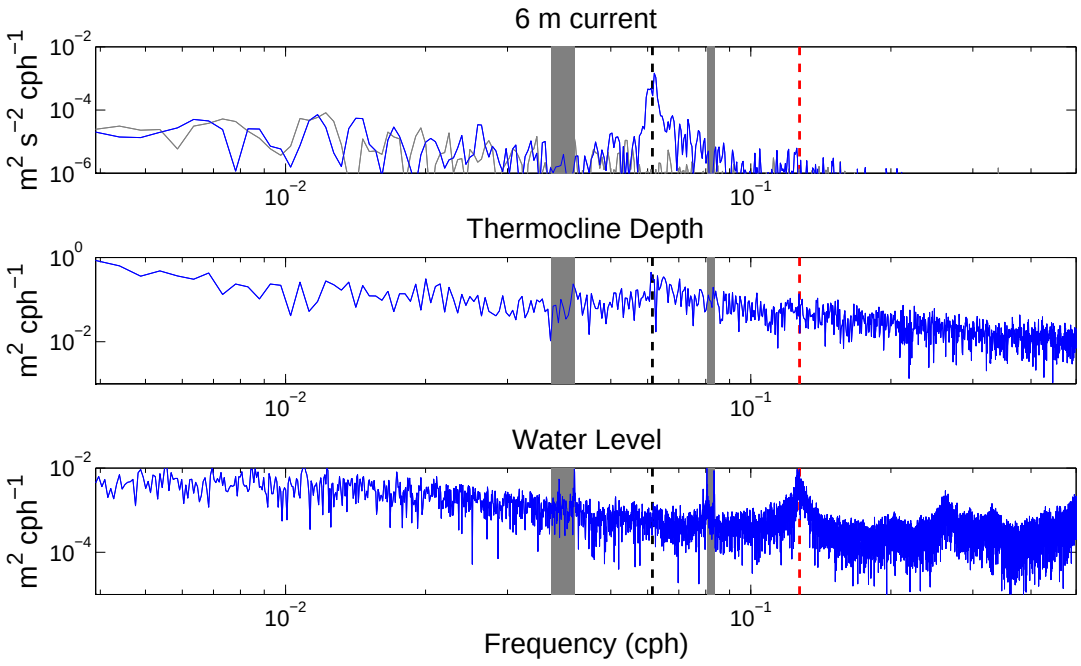

Figure 4.19: **Spectra - Observational Data.** Spectra from from observations of surface velocities, thermocline depth, and water levels during the 2011 field year. Thermocline and velocity observations were made at the western mooring site and water level records were made at NDBC station DULM5 in the Duluth, MN harbor. The black dotted line is at the local inertial frequency, the red dotted line is at the first seiche frequency and gray bars are the diurnal and semi-diurnal tidal bands.

4.3.1 Velocity Profiles

Large inertial energy is observed in surface velocities during summer and winter stratification but is weak during isothermal periods (Figure 4.20).

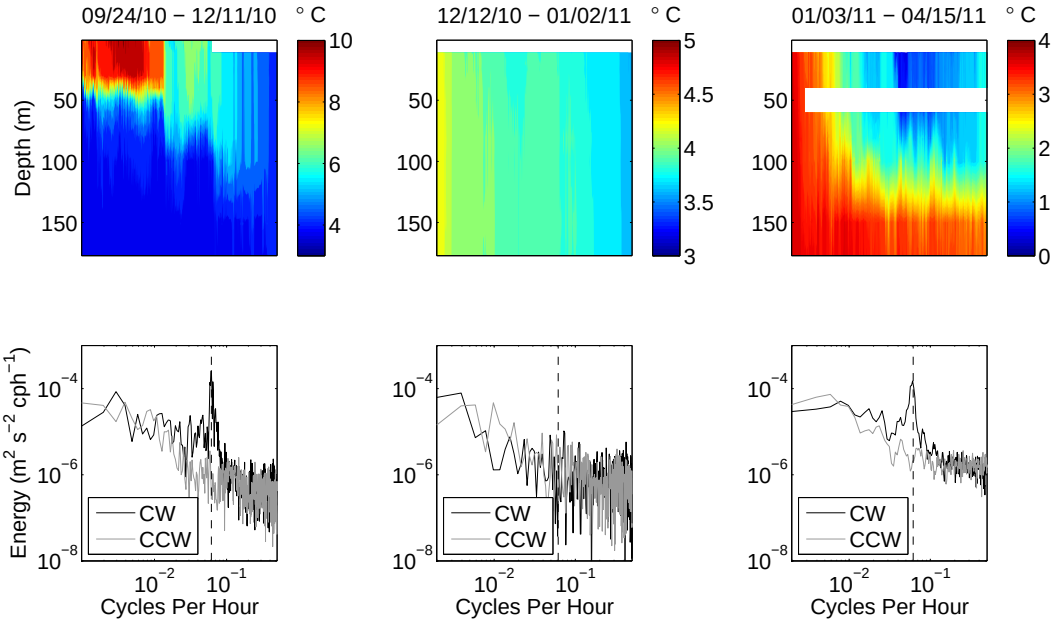

Figure 4.20: **Velocity Spectra.** Spectra of velocity during stratified and unstratified periods. The dotted line is at the Coriolis frequency.

The core mooring sites were compared during three time periods :

- June, 7 2009 - October, 4 2009
- September, 10 2010 - December, 1 2010
- June, 18 2011 - September, 19 2011

Spatial variability in the velocity magnitude is observed during each period (Figure 4.21). Interannual variability can not be properly assessed since there is little overlap in the time frames between years.

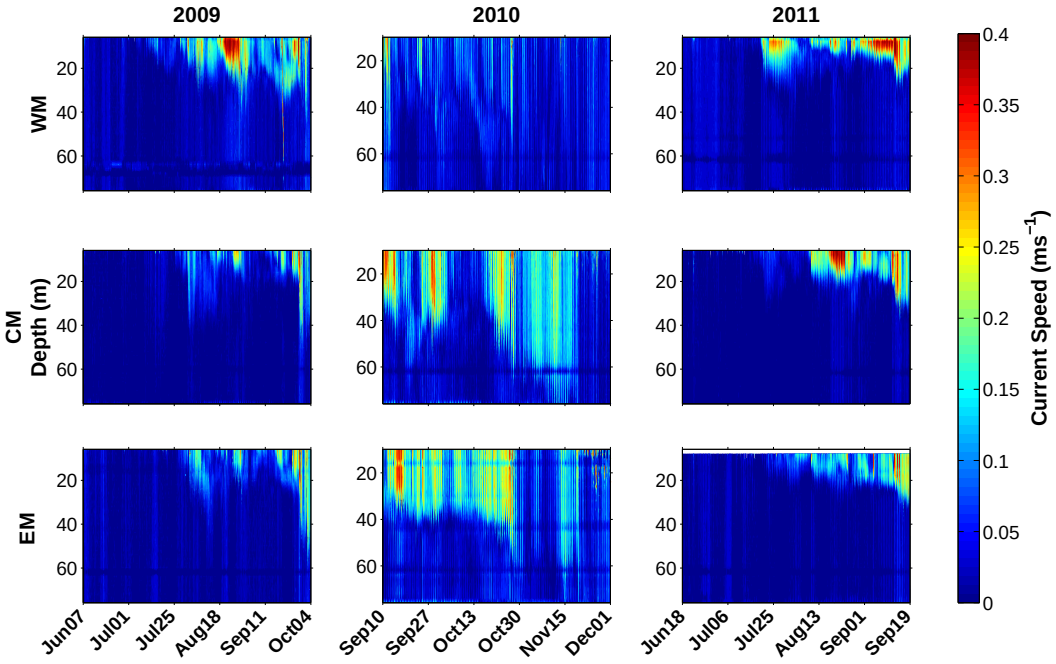

Figure 4.21: **Velocity Observations - Core Mooring Sites.** Three years worth of velocity observations at the core mooring sites, western mooring (WM), central mooring (CM), and eastern mooring (EM).

The surface velocities were averaged over the top 15 m and the time series was then convoluted with a wavelet tuned to the inertial frequency. Spatial variability was also observed in the amplitude of a clockwise wavelet power (Figure 4.22). In general, the inertial response appears to be coherent across the basin. For example, when near near-inertial energy is high at one station it is relatively high at each other station. However, inertial energy is not always high at the same location. During 2009 the inertial energy is greater at the western mooring while in 2010 there is less near-inertial energy at the western mooring compared to the other two. This suggests that there is substantial spatial variability in the energy and there is not a simple modal structure to NIWs.

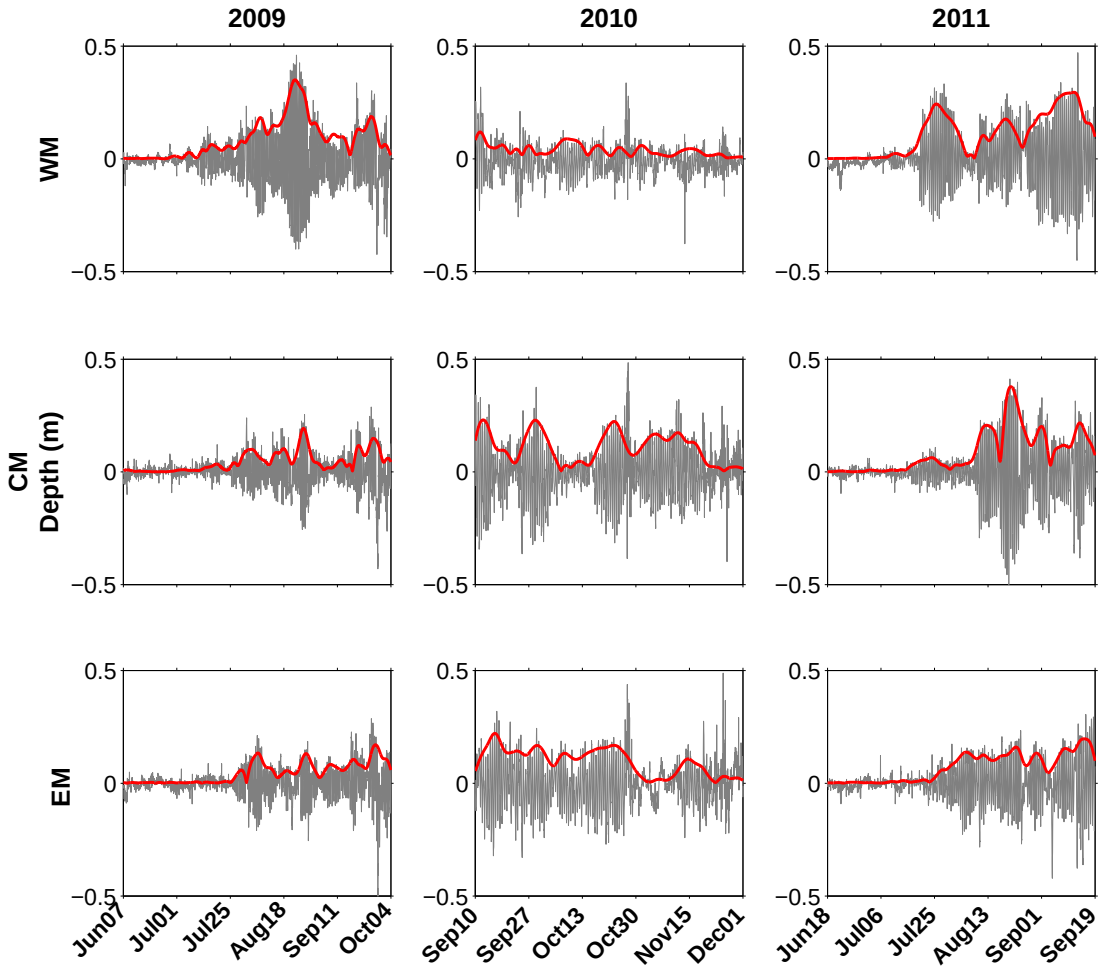

Figure 4.22: **Wavelet Amplitude - Core Mooring Sites.** The amplitude of a clockwise rotary wavelet tuned the inertial frequency during three periods.

The phase difference of the clockwise rotary wavelet tuned to the inertial frequency between two sites yields information about the phase of inertial waves. This method was applied to the core sites and reveals that the phase of the inertial wave between sites varies between -4π and 4π (Figure 4.23). This suggests that inertial waves are not coherent over the basin. There are two striking feature from this plot, one is that the western mooring (WM) and eastern mooring (EM) are are more out of phase relative to the central mooring (CM) and that the WM and and EM are more in phase with each other.

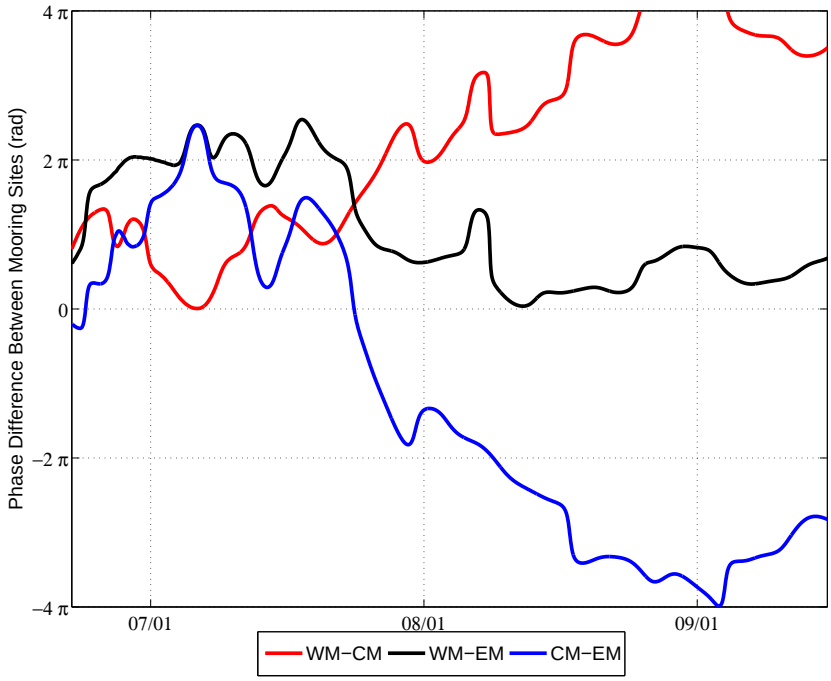

Figure 4.23: **Near-inertial Phase - Core Mooring Sites.** Phase difference between core mooring sites during the period of June 2011 - September 2011.

4.3.2 Temperature

The Western Mooring (WM) typically stratifies before the Central Mooring (CM) and Eastern Mooring (EM) since it is closer to shore and in shallow water compared to the CM and EM (Figure 4.24). Inertial waves are observed at each site during the stratified season (Figure 4.25).

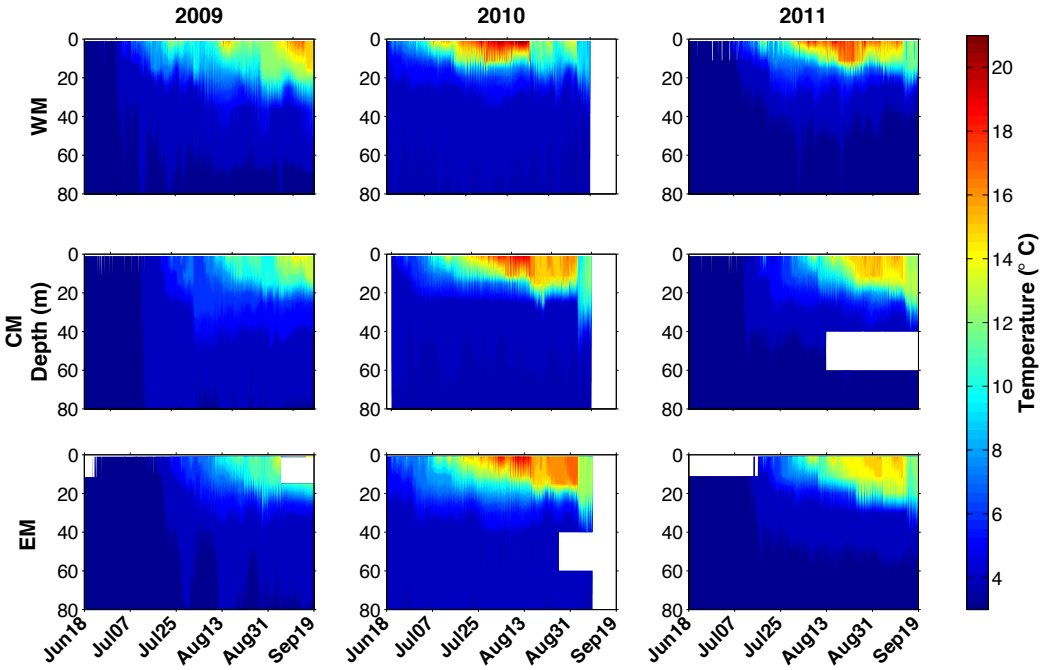

Figure 4.24: **Temperature Observations - Core Mooring Sites.** Three years worth of temperature observations at the core mooring sites, western mooring (WM), central mooring (CM), and eastern mooring (EM).

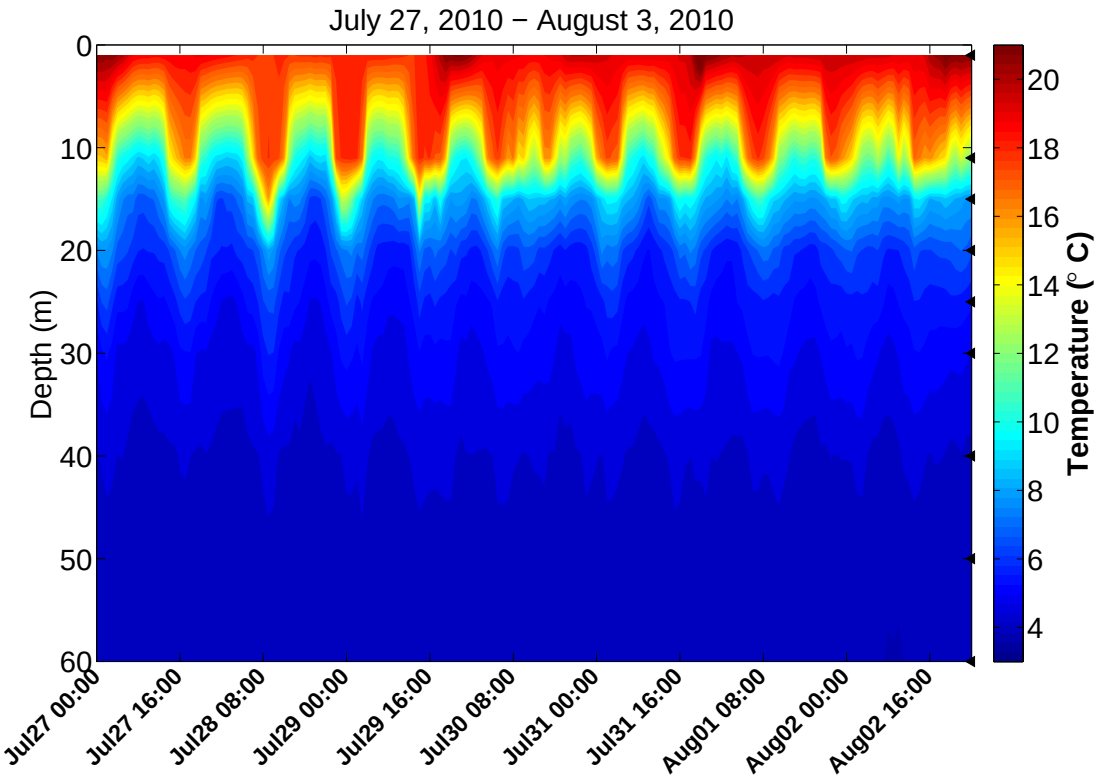

Figure 4.25: **Inertial Waves - Western Mooring.** Inertial waves are observed at the western mooring (WM) during the stratified season.

4.4 Comparison

Modeled output at the core mooring sites was compared with observational data. The timing of large velocity magnitudes in observations do not agree with the timing of large velocity magnitudes in the simulation (Figure 4.26). Also, the modeled wavelet amplitude does not agree well with the observed wavelet amplitude at each mooring (Figure 4.27 - 4.29).

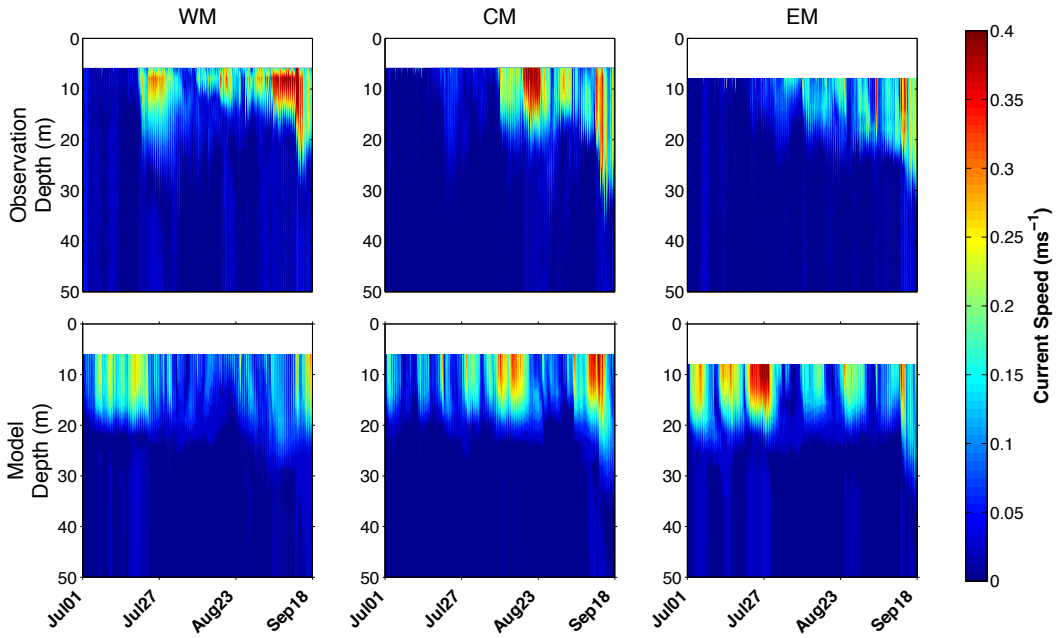

Figure 4.26: **Observational/ Model Comparison.** Comparison between velocity magnitudes at core mooring locations and approximate location in the model.

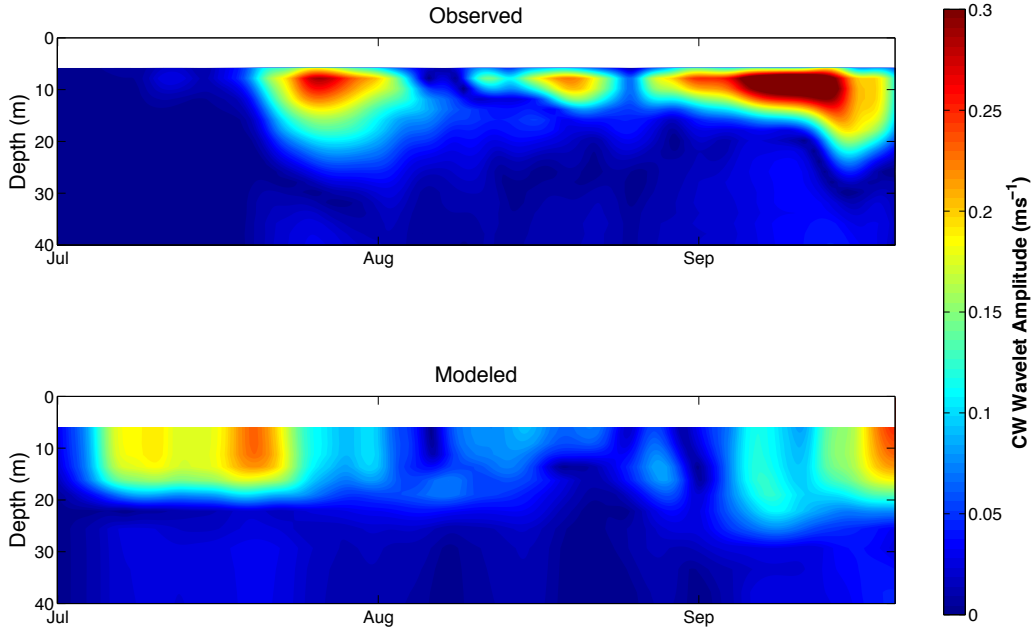

Figure 4.27: **Observational/ Modeled Wavelet Amplitude - WM.** The top plot shows the observed data between July 15, 2011 and September 15, 2011 at the western mooring while the bottom plot shows the modeled data during the same period.

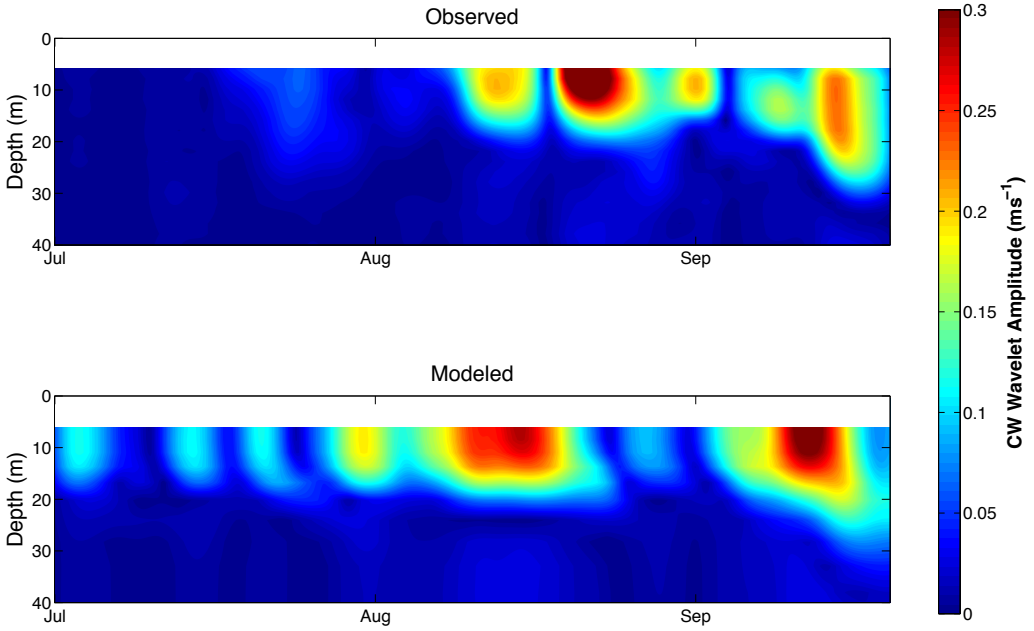

Figure 4.28: **Observational/ Modeled Wavelet Amplitude - CM.** The top plot shows the observed data between July 15, 2011 and September 15, 2011 at the central mooring while the bottom plot shows the modeled data during the same period.

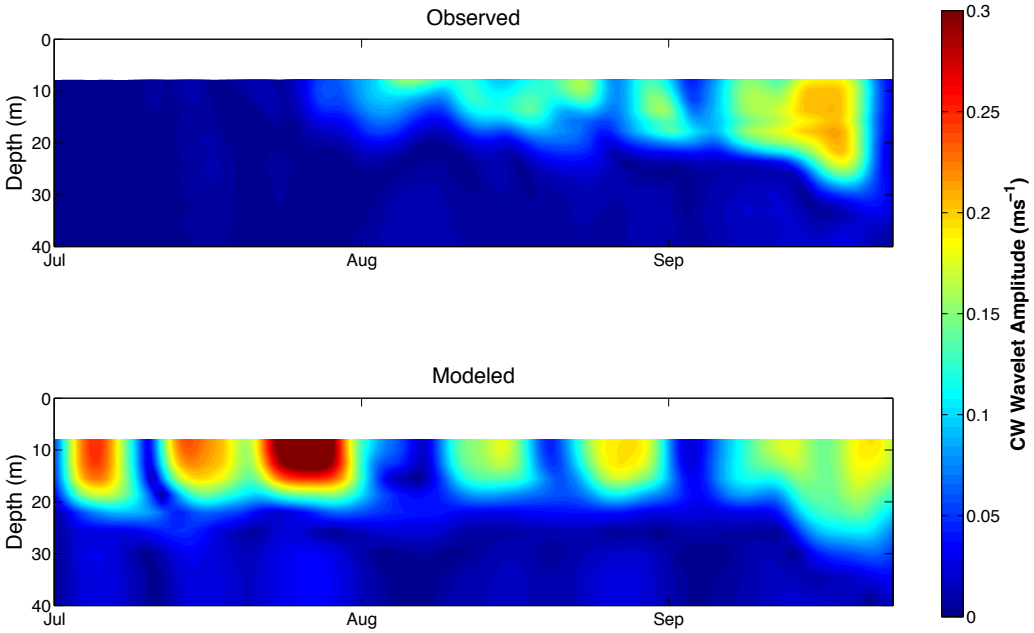

Figure 4.29: **Observational/ Modeled Wavelet Amplitude - EM.** The top plot shows the observed data between July 15, 2011 and September 15, 2011 at the eastern mooring while the bottom plot shows the modeled data during the same period.

x

Chapter 5

Discussion

5.1 Modeled Surface Wind Stress

It is difficult to accurately model near-inertial waves for a number of reasons. The kinetic energy input to the model is highly dependent on the type of forcing used. Ideal top-hat forcing for half an inertial period is efficient at putting inertial kinetic energy into surface velocities, however, top-hat forcing puts orders of magnitude less energy in outside the inertial frequency. When spatially varying forcing is used, observations and modeling agree well at low frequencies (less than or equal to inertial frequency). The modeled inertial velocities are also dependent on the phase difference between the velocity vector and wind stress vector.

5.1.1 Duration

A spectrum of model runs were done using a spatially uniform top-hat wind stress to better understand the relationship between inertial energy and the duration of forcing. The duration of the forcing varied from 1 hour up to 17 hours (approximately 1 inertial period). For each model run the magnitude of the wind stress was a constant 0.1 Nm^{-2} directed to the East. When each model run was complete a rotary spectrum was applied to the first 256 hours of output after the forced period. The inertial energy was defined as the peak in the clockwise spectrum at the inertial frequency. Top-hat forcing for half an inertial period is most efficient at putting energy into the system at the inertial frequency (Figure 5.1). The distribution of energy follows a $\sin^2(\pi t)$ curve. This curve

can be interpreted as the dot product of the inertial velocity weighted by the inertial frequency. Therefore, the inertial speed distribution follows a $\sin(\pi t)$ curve.

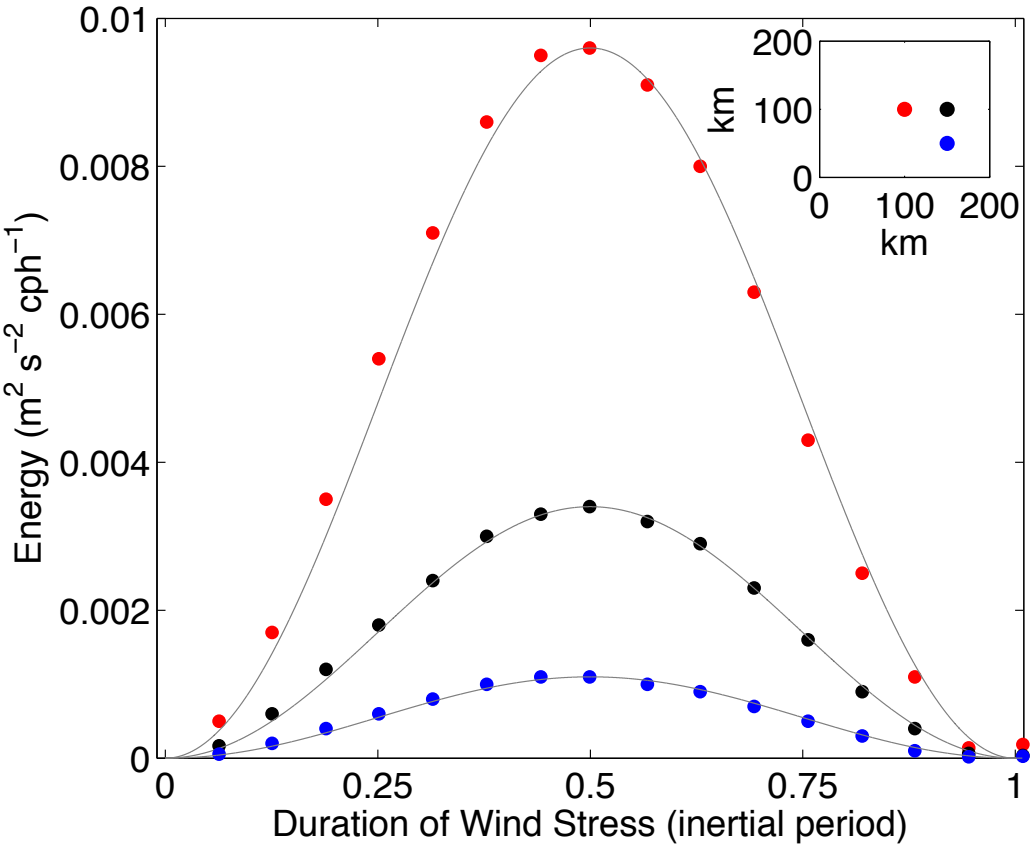

Figure 5.1: **Inertial Energy vs. Stress Duration.** Inertial energy at three locations for a spectrum of forcing durations.

Initially, the direction the wind is blowing will be the same as the direction of the surface velocity vector. The velocity vector will start to veer to the right of the velocity in the northern hemisphere (to the left of the velocity in the southern hemisphere) as a result of the Coriolis force. After half an inertial period the direction of the velocity vector will be perpendicular to the surface wind stress vector. This is the ideal time to stop the wind stress since the most momentum was put into the the surface velocity. If the ideal wind stress acts for one inertial period the inertial energy will be quelled since all the momentum put into the currents during the first half inertial period will

be removed during the second half inertial period. This idea is represented nicely with simple box model of the following set of equations :

$$\frac{du}{dt} = fv + \frac{\tau}{\rho} \tag{5.1}$$

$$\frac{dv}{dt} = fu \tag{5.2}$$

Where u and v are the zonal and meridional components of the veocity, τ is the wind stress ($\tau = 0.1$ Nm^{-2}), ρ is the density of water, and f is the inertial frequency. Stopping the forcing after half an inertial period causes the most inertial energy to remain in the system (Figure 5.2), and the inertial response is quelled when the duration of the top-hat forcing is one inertial period.

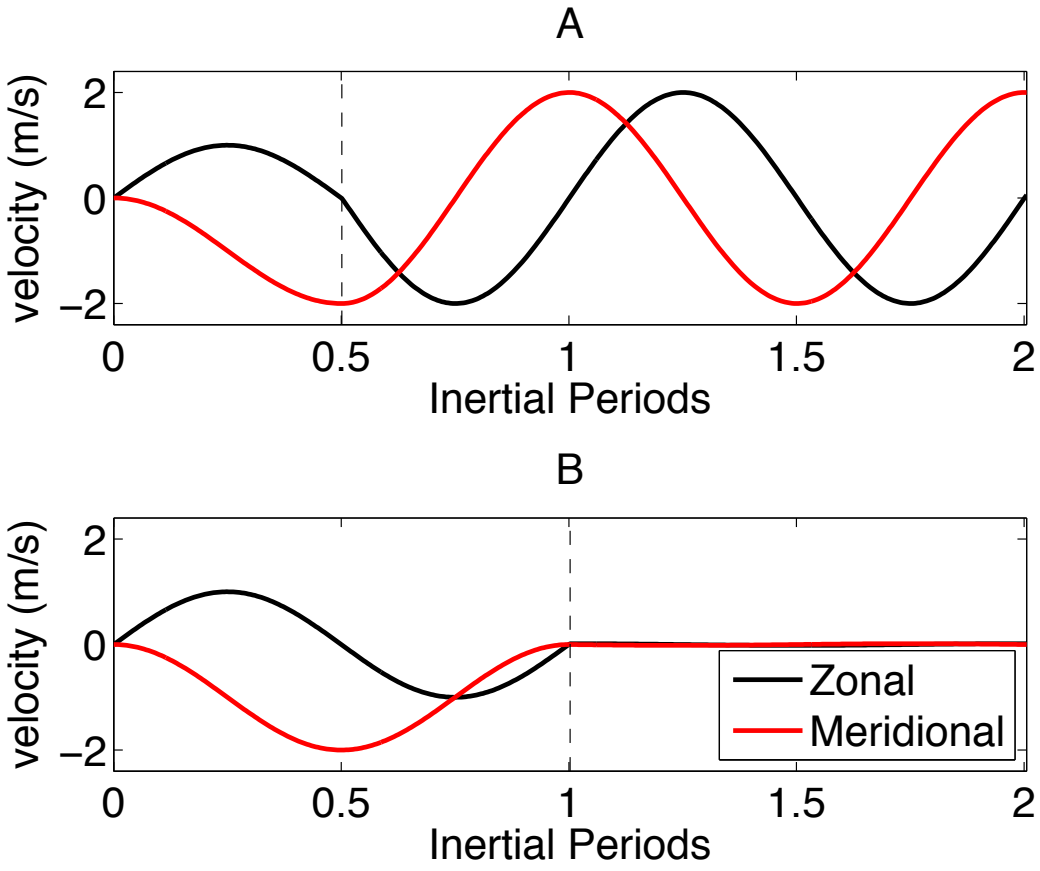

Figure 5.2: **Inertial Box Model.** Box model showing the zonal and meridional components A) when the wind stress acts for half an inertial period and B) when the wind stress acts for one inertial period. The dotted line represents the duration of the wind stress.

5.1.2 Comparison

The energy input at various frequencies is highly dependent on type of forcing used. Top-hat forcing for half an inertial period puts little energy into the system away from the inertial frequency (Figure 5.3). Top-hat wind stress and spatially varying wind stress agree well around the inertial frequency. At low frequencies the spatially varying forcing agrees quite well with observations but the ideal forcing is about four orders of magnitude lower. At high frequencies the spatially varying forcing deviates by about

one order of magnitude and the ideal forcing deviates by about four orders of magnitude. High energies outside the inertial frequency in the observations are presumably due to wind forced frequencies (Figure 5.4). This explains the reduced energy in the ideal forcing and explains why the energy is pronounced at the seiche frequencies, which are barotropic modes determined by the basin's dimensions.

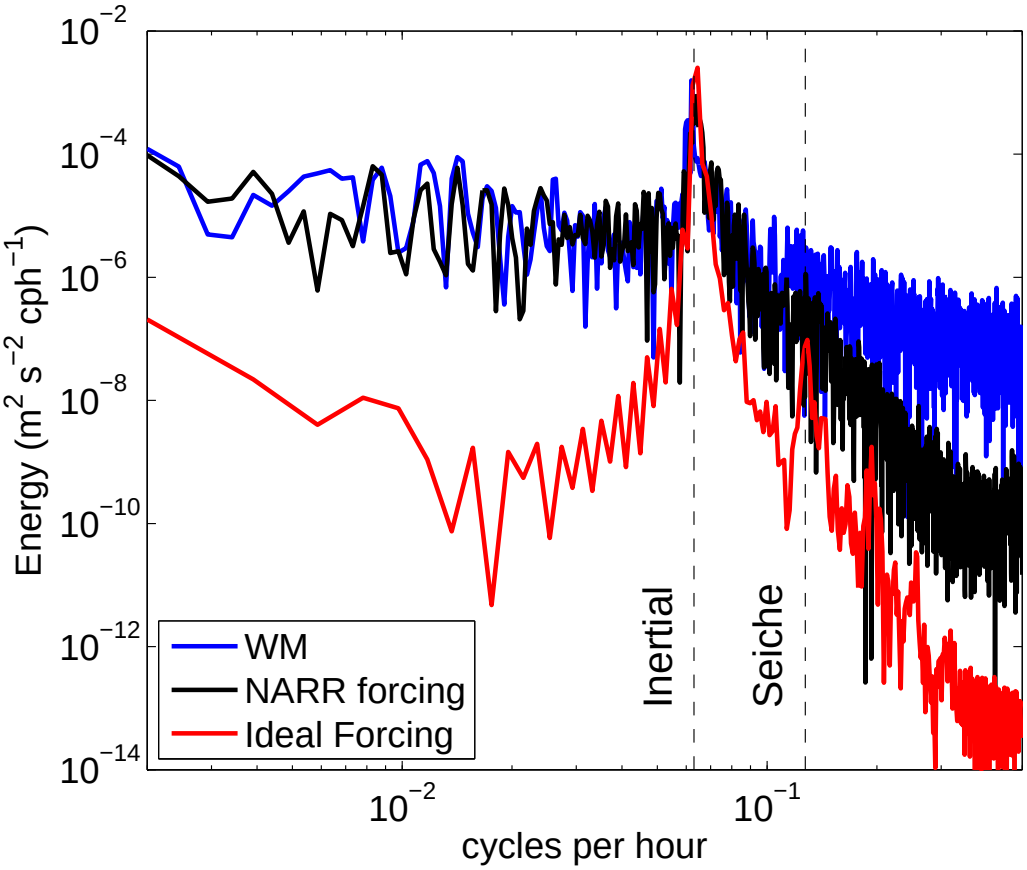

Figure 5.3: **Rotary Spectrum Comparison.** A comparison of spectra from observations at the WM, forcing derived from NARR wind speeds, and ideal forcing.

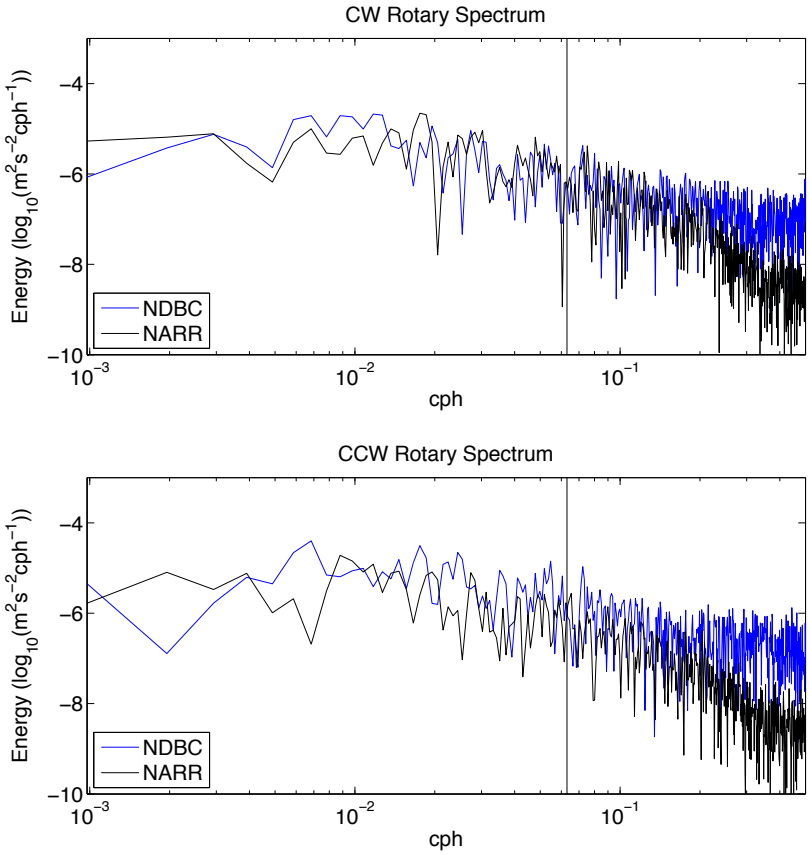

Figure 5.4: **Wind Stress Spectra.** a comparison of the clockwise (CW) and counterclockwise (CCW) rotary spectra of the observed and and modeled wind stress at the western mooring site. The solid black line is at the Coriolis frequency.

5.2 Near Inertial Waves

Near-inertial energy has large spatial and temporal variations in Lake Superior (Figure 4.22). Large spatial variability in the near-inertial energy is observed during each period. An event on July 24, 2011 put a large amount of inertial kinetic energy into currents at the western mooring, but much weaker energy at the central and eastern mooring. However, there are events that appear weakly coherent at each location. An event on August 18, 2009 put a noticeable amount of energy in the system at all stations. However, the magnitude of the event varied at each location.

5.2.1 Inertial Events

Surface wind stress can increase or decrease the kinetic energy of near-inertial currents. One can not ascertain whether energy will be put into NIWs simply by looking at a time series of wind stress because the phase difference between the velocity vector and the wind stress plays an important role. In order for the wind stress to increase the kinetic energy of the current the wind needs to be doing positive work on the currents. In other words, there must be a component of the stress in the direction of the velocity vector. Sometimes the modeled period does not coincide with observational data. For instance, an event July 24, 2011 at the western mooring put a large amount of energy into the system, (Figure 4.22), while the modeled data showed energy decreased during this time (Figure 5.5 - 5.6). The model was constantly stratified but observations show that the WM site was not stratified at the start of the modeled period. Inertial events in the model which were not significant in observations is one reason for the discrepancy between the model and observations. The inertial events prior to the onset of stratification caused the velocities in the observations and model to become out of phase and thus inertial events will have the opposite effect in the model as they do in observations. On July 23rd, 2011 before the inertial event, the phase difference between the observations and model output are close to 180°, which means the effect of the wind event will have the opposite effect in the model as it does in observations. In order to accurately model near-inertial waves the initial phase of the velocity needs to be properly assessed.

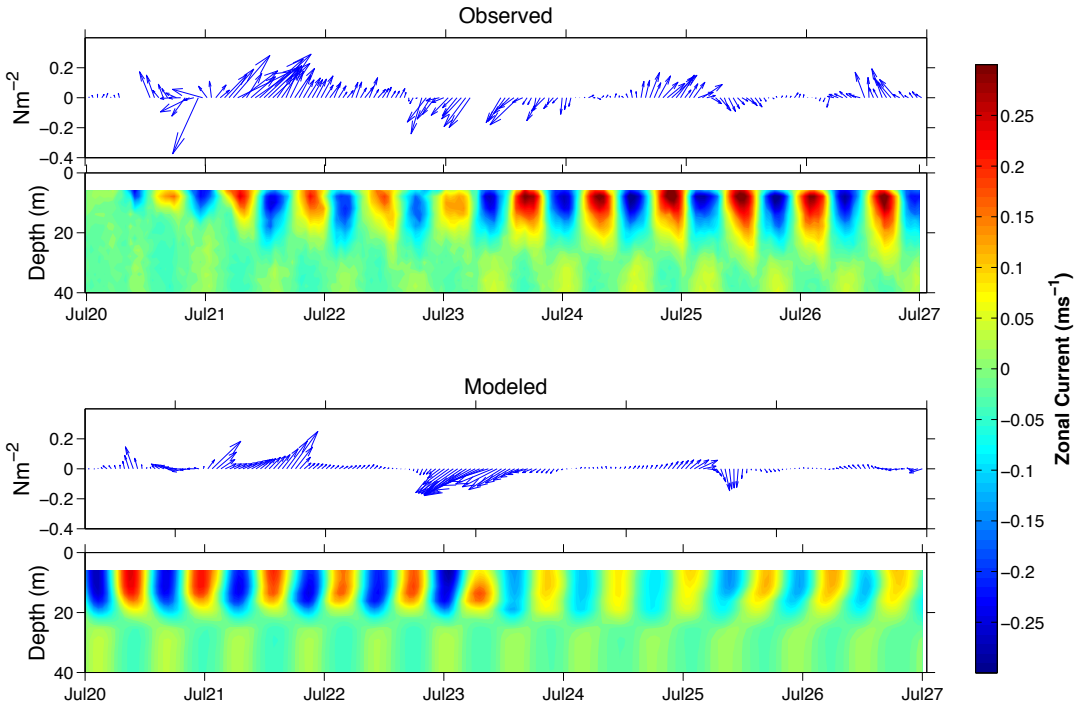

Figure 5.5: **Zonal Velocity Comparison.** Comparison between observed and modeled zonal velocities during an observed inertial event.

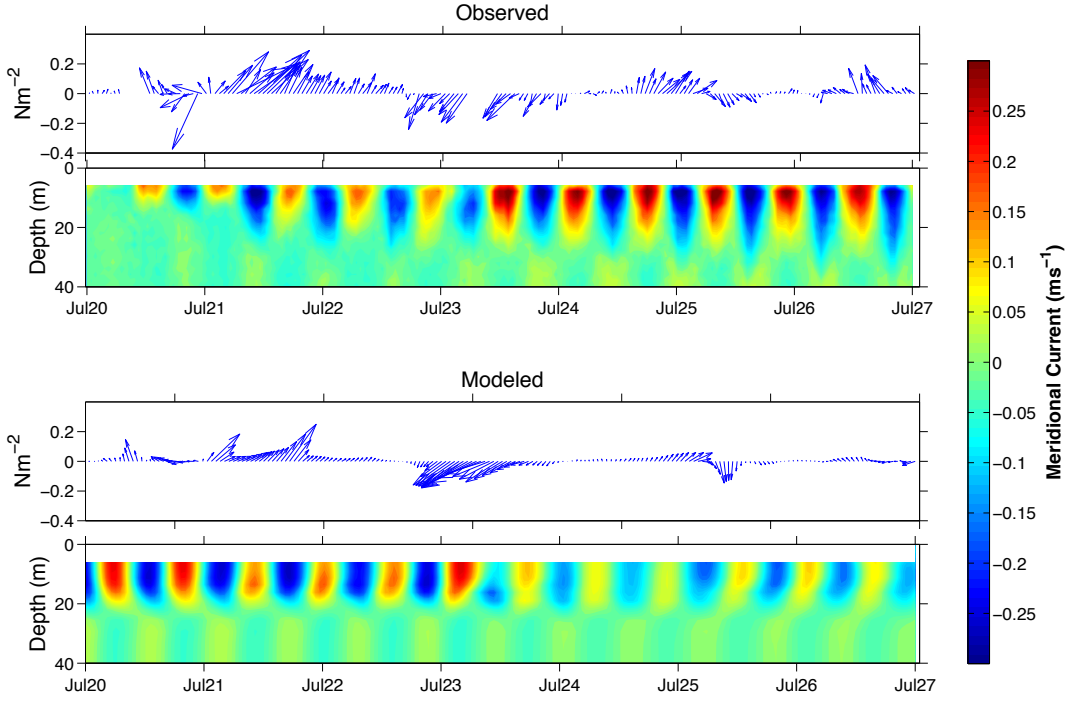

Figure 5.6: **Meridional Velocity Comparison.** Comparison between observed and modeled Meridional velocities during an observed inertial event.

5.2.2 Spatial Distribution

The spatial distribution of surface inertial energy is a function of distance from shore when flat bottom basins are forced with top-hat wind stresses. The flat bottom square basin shows high energy at the center of the basin that decreases as it approaches the shore, which is indicative of Poincaré waves. However, there is a transient period before energy stays concentrated at the center of the basin (Figure 4.5). The flat bottom Lake Superior basin shows a similar result of larger surface kinetic energy away from the coast. The distribution of energy appears to be related to distance from shore.

Bathymetry plays an important role in the distribution of surface kinetic energy in model results with real bathymetry. The spatial distribution of surface inertial kinetic energy is enhanced around shallow points in the basin when forced with spatially and temporally varying wind stress. It is unclear why energy is enhanced around these points but it may be that waves are reflecting off the bottom around these points.

5.2.3 Effect of Density Difference

The realistic simulation of Lake Superior was used to quantify the effect a small density difference has on the response at the thermocline. Realistic forcing was used in each case and the thermocline depth was set to 20 m in each simulation. The first simulation had a density difference similar to summer conditions (2.0 kg m^{-3}) and the second simulation had a density difference similar to winter conditions (0.1 kg m^{-3}). The response using summer density difference was similar at three sites in the basin (Figure 5.7). However, the response using winter conditions varied between sites.

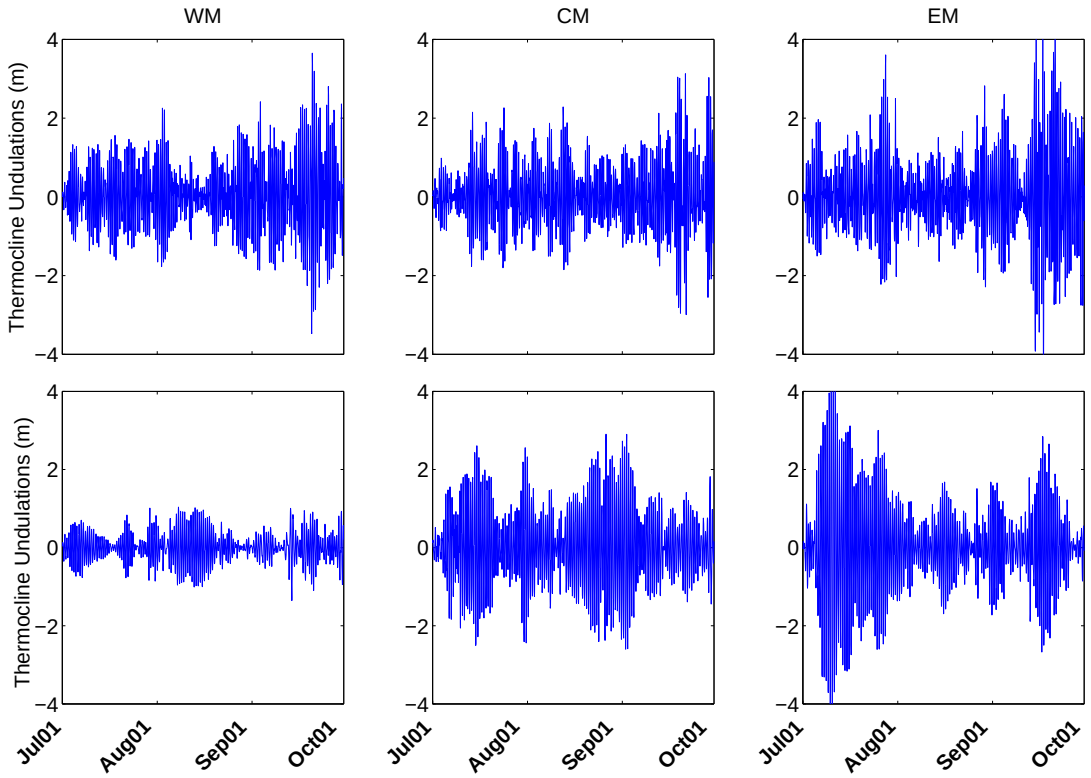

Figure 5.7: **Effect of Density Difference Across the Thermocline.** The response at the thermocline was compared using two difference density differences. The simulation in the first row had density difference of 2.0 kg m^{-3} across the thermocline while the simulation in the second row had a density difference of 0.1 kg m^{-3} across the thermocline.

5.2.4 Effect of Thermocline Depth

The realistic simulation of Lake Superior was used to quantify the effect a deeper thermocline depth has on the response at the thermocline. Realistic forcing was used in each case and the density difference across the interface was the same in each case. The first simulation has the thermocline depth similar to summer conditions (20m) and the second simulations had a thermocline depth similar to winter conditions (100m). The effect of pushing the thermocline deeper into the water column decreased the response at the thermocline (Figure 5.8). This result was expected since there is a deeper column of water overlying the thermocline. Therefore, more water needs to be accelerated.

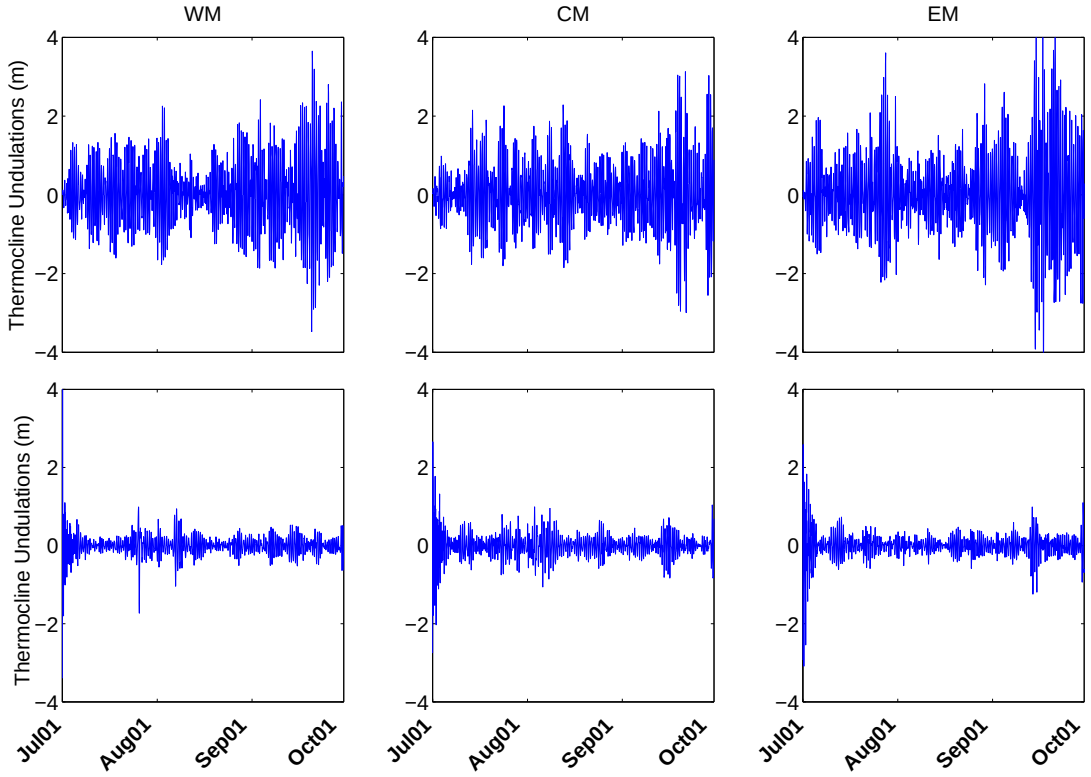

Figure 5.8: **Effect of Thermocline Depth.** The response at the thermocline was compared using two thermocline depths. The simulation in the first had a thermocline depth of 20 m while the simulation in the second row had a thermocline depth of 100 m.

5.3 Model Equations

The two layer equations model equations (A.3) yield some unique properties of inertial waves. The two layer model equations are :

Top Layer Solutions

$$u_1 = u_{10}\cos(kx - \omega t)$$
$$v_1 = \frac{f}{\omega}u_{10}\sin(kx - \omega t)$$

Bottom Layer Solutions

$$u_2 = -\frac{h_1}{h_2}u_{10}\cos(kx - \omega t)$$
$$v_2 = -\frac{h_1}{h_2}\frac{f}{w}u_{10}\sin(kx - \omega t)$$

Free Surface Displacement

$$\eta_1 = 0$$
$$\eta_2 = -\frac{h_1 k}{\omega}u_{10}\cos(kx - \omega t)$$

Notice that the zonal components in the top and bottom layer (u_1 and u_2) are 180° out of phase, which is indicative of a baroclinic mode. Likewise, the meridional components (v_1 and v_2) in the top and bottom layer (u_1 and u_2) are 180° out of phase. The magnitude of the zonal and meridional components in the bottom layer are multiplied by $\frac{h_1}{h_2}$, this factor is less than one and acts to decrease the magnitude of the velocity in the bottom layer. This solution explains why larger velocity magnitudes are observed near the shore and over the Keweenaw ridge. The model equations also imply the velocity vectors are rotating clockwise in the top and bottom layer. The eccentricity of the inertial orbit is given by $\frac{f}{\omega}$. An eccentricity of one, or $f = \omega$, implies a circular orbit. However, near-inertial waves have frequencies slightly greater than the inertial frequency. Therefore, the eccentricity will be nearly circular.

5.3.1 Wave Climate

The wavelength and direction of propagation of NIWs were estimated following the same procedure as Austin (2013). Austin (2013) estimated the wavelength of NIWs to be between 30 km and 60 km during a large event at the end of July 2010. A large inertial event also occurred near the end of July 2011. The calculated wavelength during this period was calculated to be around 60 km, Figure (4.16). However, for most of the modeled period the wavelength is above 100 km. The modeled period also shows a

slow counter-clockwise rotation with a period of about 30 days in the NIWs direction of propagation at all the mooring sites, Figure (4.16). Austin (2013) calculated a similar result and noted that this period is on the same order as the lowest order internal Kelvin wave. The Kelvin wave phase speed can not be accurately modeled with the current model configuration since the horizontal resolution is greater than 20% of the Rossby radius (Schwab and Beletsky 1998).

Chapter 6

Conclusions

6.1 Conclusions

Conclusions from simulations with an ideal basin :
1) The input of momentum to surface currents is highly dependent on the duration of idealized forcing. An idealized wind stress lasting for half an inertial period is most efficient putting momentum into surface currents. An idealized wind stress lasting for one inertial period will not add any momentum to the surface currents.
2)Using doubly periodic boundary conditions showed that a divergence in flow, such as at a coast, is necessary to initiate internal waves

Conclusions from simulations with a Lake Superior basin :
1) Modeling Lake Superior with a uniform bathymetry showed that inertial energy is greatest offshore and weakest at the coast.
2) Modeling Lake Superior with realistic bathymetry showed that inertial energy is amplified over the Superior shoal. This may be related to internal waves reflecting and converging over the shoal.

Modeling with idealized forcing (with a duration of half an inertial period) adds a substantial amount of energy to surface currents in the inertial frequency band. Compared to observations, idealized forcing puts little energy into frequencies above or below the inertial band. Model output using forcing derived from NARR climatology output compares well with observations. However, energy input using NARR forcing drops off substantially at frequencies greater than the Nyquist frequency ($\frac{1}{6}$ hr^{-1}).

The two parameters that change the internal Rossby radius of deformation are the vertical stratification scale (thermocline depth) and the density difference across the thermocline. The response at the thermocline as a result of decreasing the density difference varies spatially. However, the response at the thermocline as a result of increasing the vertical stratification scale is weak at the three mooring sites. This suggest thats there is a non-trivial relationship between the response at the thermocline and the density difference across the thermocline. Additional work is needed to explain the spatial variability in the response as a result of decreasing the density difference.

In order to accurately simulate inertial events the phase difference between the velocity and wind stress needs to be correct. In order to increase the magnitude of the velocity the wind stress needs to be doing positive work on the currents. This happens when a component of the wind stress is in the same direction as the velocity.

6.2 Future Work

Accurately simulating inertial events is difficult since the phase of the velocity relative to the wind stress needs to be correct. In order to better understand near-inertial currents in Lake Superior a more realistic model is needed. Here are two possible ways to improve the model.

1) add surface heat fluxes to the model so the thermal structure can evolve on its own.
2) update the model at each time step with observed thermal structure.

Observations have suggested that near-inertial waves may be an important driver resuspending sediment (Austin 2013). The relationship between near-inertial waves and sediment resuspension is still an active area of research and is important because these waves may transport nutrients as well. Although NIWs have been correlated with the thickness of the bottom nephoid layer (Hawley 2004) the relationship has not been quantified. For example, what will the thickness of the bottom nephoid layer be after an inertial event?

This thesis has shown that near-inertial currents are enhanced over the the Superior shoal. The mechanism enhancing near-inertial currents in this region is still unclear. However, it was suggested that this may be due to reflected internal waves converging atop the shoal.

This thesis showed that the duration of a wind event is important and that the phase difference between velocity and wind stress is important for the input or removal of near-inertial energy. However, this thesis did not address which type of synoptic weather systems initiate near-inertial currents in Lake Superior. This type of work has been done in the coastal ocean comparing near-inertial events to synoptic weather charts (D'Asaro 1985). Another useful measure would be to map the wind power input across the Lake Superior basin.

This thesis suggests there is a non-trivial relationship between near-inertial response at the thermocline and the density difference across the thermocline. The response varies at the three sites. Additional work in this area is needed to address this non-trivial response.

Near-inertial currents dominate Lake Superior during the stratified season and understanding the structure of these waves and events that trigger them has ecological significance. Although it is difficult to accurately simulate inertial events it is possible to make statistical predictions of the NIW climate.

References

Ahmed, S., Troy, C. D., and Hawley, N. 2013. Spatial structure of internal poincaré waves in lake michigan. *Environmental Fluid Mechanics*. doi: 10.1007/s10652-013-9294-3.

Antenucci, J. and Imberger, J. 2001. Energetics of long internal gravity waves in large lakes. *Limnol. Oceanogr.*, 46(7):1760:1773.

Austin, J. 2013. Observations of near-inertial energy in lake superior. *Limnol. Oceanogr.*, 58(2):715–728. doi:10.4319/lo.2013.58.2.0715.

Austin, J. A. and Allen, J. 2011. Sensitivity of summer lake superior thermal structure to meteorological forcing. *Limnology and Oceanography*, 56(3):1141–1154.

Austin, J. A. and Colman, S. M. 2007. Lake superior summer water temperatures are increasing more rapidly than regional air temperatures: A positive ice-albedo feedback. *Geophysical Research Letters*, 34:6604.

Blanton, J. 1974. Some characteristics of nearshore currents along the north shore of lake ontario. *Journal of Physical Oceanography*, 4(3):415–424.

Bouffard, D., Boegman, L., Ackerman, J. D., Valipour, R., and Rao, Y. R. 2014. Near-inertial wave driven dissolved oxygen transfer through the thermocline of a large lake. *Journal of Great Lakes Research*, 40(2):300–307.

Boyce, F., Donelan, M., Hamblin, P., Murthy, C., and Simons, T. 1989. Thermal structure and circulation in the great lakes. *Atmosphere-ocean*, 27(4):607–642.

Boyce, F. M. and Chiocchio, F. 1987. Inertial frequency current oscillations in the central basin of lake erie. *J. Great Lakes. Res.*, 13(4):542–558.

Bugnon, F. and Whitehouse, I. 1991. Acoustic doppler current meter. *Oceanic Engineering, IEEE Journal of*, 16(4):420–426.

Chen, C.-T. and Millero, F. J. 1986. Precise thermodynamic properties for natural waters covering only the limnological range. *Limnology and Oceanography*, 31(3): 657–662.

Choi, J., Troy, C. D., Hsieh, T.-C., Hawley, N., and McCormick, M. J. 2012. A year of internal poincaré waves in southern lake michigan. *Journal of Geophysical Research: Oceans (1978–2012)*, 117(C7).

D'Asaro, E. A. 1985. The energy flux from the wind to near-inertial motions in the surface mixed layer. *Journal of Physical Oceanography*, 15(8):1043–1059.

Ekman, V. 1904. On dead-water. norw. n. polar exped. 1893-1896: Sci. results. *Christiania XV*.

Fairall, C. W., Bradley, E. F., Rogers, D. P., Edson, J. B., and Young, G. S. 1996. Bulk parameterization of air-sea fluxes for tropical ocean-global atmosphere coupled-ocean atmosphere response experiment. *Journal of Geophysical Research*, 101(C2): 3747–3764.

Glover, D. M., Jenkins, W. J., and Doney, S. C. *Modeling methods for marine science*. Cambridge University Press, 2011.

Gómez-Giraldo, A., Imberger, J., and Antenucci, J. P. 2006. Spatial structure of the dominant basin-scale internal waves in lake kinneret. *Limnology and oceanography*, 51(1):229.

Graney, C. M. 2011. Coriolis effect, two centuries before coriolis. *Physics Today*, 64(8): 8–9.

Hawley, N. 2004. Response of the benthic nepheloid layer to near-inertial internal waves in southern lake michigan. *J. Geophys. Res.*, 109:C04007. doi:10.1029/2003JC002128.

Kundu, P. and Cohen, I. Fluid mechanics. fourth edition, 2008.

Kundu, P. K., Chao, S.-Y., and McCreary, J. P. 1983. Transient coastal currents and inertio-gravity waves. *Deep Sea Research Part A. Oceanographic Research Papers*, 30 (10):1059–1082.

Marmorino, G. O. 1978. Inertial current in lake ontario, winter 1972-73 (ifygl). *Journal of Physical Oceanography*, 8(6):1104–1120.

McCulloch, J. 1973. The international field year for the great lakes. *Hydrological Sciences Journal*, 18(3):367–373.

Millot, C. and Crépon, M. 1981. Inertial oscillations on the continental shelf of the gulf of lions-observations and theory. *Journal of Physical Oceanography*, 11(5):639–657.

Mortimer, C. H. 1974. Lake hydrodynamics.

Niirnberg, G. K. 1995. Quantifying anoxia in lakes. *Limnology and Oceanography*, 40 (6):1100–1111.

Pickett, R. and Richards, F. 1975. Lake ontario mean temperatures and currents in july 1972. *Journal of Physical Oceanography*, 5(4):775–781.

Pollard, R. T. 1970. On the generation by winds of inertial waves in the ocean. *Deep-Sea Res.*, 17:795–812.

Pollard, R. T. and Millard Jr., R. C. 1970. Comparison between observed and simulated wind-generated inertial oscillations. *Deep-Sea Res.*, 17:813–821.

Qi, H., De Szoeke, R. A., Paulson, C. A., and Eriksen, C. C. 1995. The structure of near-inertial waves during ocean storms. *Journal of Physical Oceanography*, 25(11): 2853–2871.

Quinn, F. H. 1992. Hydraulic residence times for the laurentian great lakes. *Journal of Great Lakes Research*, 18(1):22–28.

Rao, D. B. and Schwab, D. J. 1976. Two dimensional normal modes in arbitrary enclosed basins on a rotating earth: Application to lakes ontario and superior. *Philosophical*

Transactions of the Royal Society of London. Series A, Mathematical and Physical Sciences, 281(1299):63–96.

Rott, N. 1990. Note on the history of the reynolds number. *Annual review of fluid mechanics*, 22(1):1–12.

Rueda, F. J., Schladow, S. G., and Pálmarsson, S. Ó. 2003. Basin-scale internal wave dynamics during a winter cooling period in a large lake. *Journal of Geophysical Research: Oceans (1978–2012)*, 108(C3).

Schwab, D. J. 1977. Internal free oscillations in lake ontario. *Limnol. Oceanogr*, 22(4): 700–708.

Schwab, D. J. and Beletsky, D. 1998. Propagation of kelvin waves along irregular coastlines in finite-difference models. *Advances in water resources*, 22(3):239–245.

Schwab, D. J. and Sellers, D. L. *Computerized bathymetry and shorelines of the Great Lakes*. National Oceanographic and Atmospheric Administration, US Department of Commerce, Great Lakes Environmental Research Laboratory, 1996.

Shearman, R. K. 2005. Observations of near-inertial current variability on the new england shelf. *Journal of Geophysical Research: Oceans (1978–2012)*, 110(C2).

Sloss, P. W. and Saylor, J. H. 1976. Large-scale current measurements in lake huron. *Journal of Geophysical Research*, 81(18):3069–3078.

Thomas, R. and Dell, C. 1978. Sediments of lake superior. *Journal of Great Lakes Research*, 4(3):264–275.

Webster, F. 1968. Observations of inertial-period motions in the deep sea. *Reviews of Geophysics*, 6(4):473–490.

Appendix A

Solving Momentum Equations

A.1 Pure Inertial

The pure inertial Navier-Stokes equation for the velocity and position function are as follows :

$$\frac{du}{dt} - fv = 0 \tag{A.1}$$

$$\frac{dv}{dt} + fu = 0 \tag{A.2}$$

Differentiate equation (A.1) with respect to time :

$$\frac{d^2u}{dt^2} - f\frac{dv}{dt} = 0 \tag{A.3}$$

Equation (A.2) can be written as :

$$\frac{dv}{dt} = -fu \tag{A.4}$$

Equation (A.4) can be substituted into equation (A.3) :

$$\frac{d^2u}{dt^2} - f\frac{dv}{dt} = 0 \tag{A.5}$$

$$\frac{d^2u}{dt^2} + f^2u = 0 \tag{A.6}$$

$$\frac{d^2u}{dt^2} = -f^2u \tag{A.7}$$

$$u(t) = u_o \cos(ft + \phi) \tag{A.8}$$

Equation (A.8) can substituted into equation (A.1) and solved for $v(t)$:

$$\frac{du}{dt} - fv = 0 \tag{A.9}$$

$$\frac{d(u_o \cos(ft + \phi))}{dt} - fv = 0 \tag{A.10}$$

$$fv = -u_o f \sin(ft + \phi) \tag{A.11}$$

$$v(t) = -u_o \sin(ft + \phi) \tag{A.12}$$

The components of the velocity field are given by :

$$u(t) = u_o \cos(ft + \phi) \tag{A.13}$$

$$v(t) = -u_o \sin(ft + \phi) \tag{A.14}$$

Integrating over time yields expressions for the equations of motion :

$$x(t) = \int_0^t u(t')dt' = \int_0^t u_o \cos(ft' + \phi)dt' = \frac{u_o}{f}\sin(ft + \phi) + x_o \tag{A.15}$$

$$y(t) = \int_0^t v(t')dt' = \int_0^t -u_o \sin(ft' + \phi)dt' = \frac{u_o}{f}\cos(ft + \phi) + y_o \tag{A.16}$$

A.2 Single Layer

Single layer momentum equations is as follows :

$$\frac{du}{dt} - fv = -g\frac{d\eta}{dx} \tag{A.17}$$

$$\frac{dv}{dt} + fu = -g\frac{d\eta}{dy} \tag{A.18}$$

$$\frac{dw}{dt} + g = -g\frac{d\eta}{dz} \tag{A.19}$$

The continuity equation is as follows :

$$h\left(\frac{du}{dx} + \frac{dv}{dy}\right) + \frac{d\eta}{dt} = 0 \tag{A.20}$$

A plane wave solution of the following form will be applied to equations (B.1) - (B.4) :

$$(u, v, \eta) \sim (u_o, v_o, \eta_o) \exp i(kx - \omega t) \tag{A.21}$$

Without loss of generality we will assume the wave is propagating in the x direction. This yields the following set of equations :

$$-\omega ui + -fv + gk\eta i = 0 \tag{A.22}$$

$$fu - \omega vi = 0 \tag{A.23}$$

$$h_1 kui - \omega\eta i = 0 \tag{A.24}$$

From Equation A.24 we can write :

$$u = \frac{\omega}{h_1 k}\eta \tag{A.25}$$

$$v = \frac{f}{\omega i}u = \frac{f}{h_1 ki}\eta = -\frac{fi}{h_1 k}\eta \tag{A.26}$$

The surface displacement can be written in the following form :

$$\eta(t) = \eta_o(\cos(kx - \omega t) + i\sin(kx - \omega t)) \tag{A.27}$$

This can be substituted into Equation A.26 to get:

$$u(t) = \frac{\omega}{hk}\eta_o \cos(kx - \omega t) \tag{A.28}$$

$$\tag{A.29}$$

$$v(t) = \frac{f}{hk}\eta_o \sin(kx - \omega t) \tag{A.30}$$

$$\tag{A.31}$$

Integrating Equation A.29 and Equation A.30 over time yields :

$$x(t) = \int u(t)dt = \int \frac{\omega}{hk}\eta_o \cos(kx - \omega t)dt = -\frac{\eta_o}{hk}\sin(kx - \omega t) \tag{A.32}$$

$$y(t) = \int v(t)dt = \int \frac{f}{hk}\eta_o \sin(kx - \omega t)dt = \frac{f}{hk\omega}\eta_o \cos(kx - \omega t) \tag{A.33}$$

Only the real component has any physical meaning, since we are confining the propagation to the x direction. A summary of the single layer model equations is provided below.

Velocity Components

$$u(t) = \frac{\omega}{hk}\eta_o \cos(kx - \omega t)$$

$$v(t) = \frac{f}{hk}\eta_o \sin(kx - \omega t)$$

Position Components

$$x(t) = -\frac{\eta_o}{hk}\sin(kx - \omega t)$$

$$y(t) = \frac{f}{hk\omega}\eta_o \cos(kx - \omega t)$$

Free Surface Displacement

$$\eta(t) = \eta_o \cos(kx - \omega t)$$

A.3 Double Layer

The momentum equation for a two layer system, assuming a rigid lid approximation, are as follows :

Top Layer	**Bottom Layer**
$\frac{du_1}{dt} - fv_1 = -g\frac{d\eta_1}{dx}$	$\frac{du_2}{dt} - fv_2 = -g'\frac{d\eta_2}{dx} - g\frac{d\eta_1}{dx}$
$\frac{dv_1}{dt} + fu_1 = -g\frac{d\eta_1}{dy}$	$\frac{dv_2}{dt} + fu_2 = -g'\frac{d\eta_2}{dy} - g\frac{d\eta_1}{dy}$
$h_1\left(\frac{du_1}{dx} + \frac{dv_1}{dy}\right) + \frac{d\eta_1}{dt} - \frac{d\eta_2}{dt} = 0$	$h_2\left(\frac{du_2}{dx} + \frac{dv_2}{dy}\right) + \frac{d\eta_2}{dt} = 0$

The following plane wave solution was applied to the latter momentum equations :

$$(u, v, \eta) \sim (u_o, v_o, \eta_o) \exp i(kx - \omega t) \tag{A.34}$$

Applying a plane wave solution yields the following set of equations :

Top Layer	**Bottom Layer**
$-i\omega u_1 - fv_1 = -igk\eta_1$	$-i\omega u_2 - fv_2 = -g'ik\eta_2 - gik\eta_1$
$-i\omega v_1 + fu_1 = 0$	$-i\omega v_2 + fu_2 = 0$
$h_1(iku_1) - i\omega\eta_1 + i\omega\eta_2 = 0$	$h_2(iku_2) - i\omega\eta_2 = 0$

The general solution for the zonal velocity in the top layer can be written as :

$$u(t) = u_o(\cos(kx - \omega t) + i\frac{f}{\omega}\sin(kx - \omega t)) \tag{A.35}$$

The second momentum equation in the top layer can be solved for $v(t)$:

$$-i\omega v_1 + fu_1 = 0 \tag{A.36}$$

$$v_1 = \frac{f}{i\omega}u_1 \tag{A.37}$$

$$v_1 = -\frac{fi}{\omega}u_1 \tag{A.38}$$

$$v_1 = -\frac{fi}{\omega}u_o(\cos(kx - \omega t) + i\sin(kx - \omega t)) \tag{A.39}$$

$$v_1 = \frac{f}{\omega}u_o(-i\cos(kx - \omega t) + \sin(kx - \omega t)) \tag{A.40}$$

An expression for η_2 can be found from the continuity equation in the top layer, assuming $\eta_1 = 0$:

$$h_1(iku_1) - i\omega\eta_1 + i\omega\eta_2 = 0 \tag{A.41}$$

$$h_1 k u_1 + \omega\eta_2 = 0 \tag{A.42}$$

$$\eta_2 = -\frac{h_1 k}{\omega} u_1 \tag{A.43}$$

$$\eta_2 = -\frac{h_1 k}{\omega} u_o(\cos(kx - \omega t) + i\sin(kx - \omega t)) \tag{A.44}$$

$$\tag{A.45}$$

An expression for u_2 can be found from the continuity equation in the bottom layer :

$$h_2(iku_2) - i\omega\eta_2 = 0 \tag{A.46}$$

$$u_2 = \frac{\omega}{h_2 k}\eta_2 \tag{A.47}$$

$$u_2 = -\frac{\omega}{h_2 k}\frac{h_1 k}{\omega} u_o(\cos(kx - \omega t) + i\sin(kx - \omega t)) \tag{A.48}$$

$$u_2 = -\frac{h_1}{h_2} u_o(\cos(kx - \omega t) + i\sin(kx - \omega t)) \tag{A.49}$$

$$\tag{A.50}$$

Expression for v_2 can be found from the second momentum equation in bottom layer :

$$-i\omega v_2 + f u_2 = 0$$

$$v_2 = \frac{f}{i\omega} u_2$$

$$v_2 = -\frac{f}{i\omega}\frac{h_1}{h_2} u_o(\cos(kx - \omega t) + i\sin(kx - \omega t))$$

$$v_2 = \frac{f}{\omega}\frac{h_1}{h_2} u_o(i\cos(kx - \omega t) - \sin(kx - \omega t))$$

From the continuity equation in the top layer we can show that $\eta_1 = 0$, assuming a rid lid :

$$h_1(iku_1) - i\omega\eta_1 + i\omega\eta_2 = 0$$

$$\eta_1 = \eta_2 + \frac{h_1 k}{\omega} u_1$$

$$\eta_1 = -\frac{h_1 k}{\omega} u_{10} \cos(kx - \omega t) + \frac{h_1 k}{\omega} u_{10} \cos(kx - \omega t)$$

$$\eta_1 = 0$$

Since we are assuming the wave is propagating solely in the x direction then only the real solution has any physical meaning. A summary of the two layer model equations is provided below.

Top Layer Solutions

$$u_1 = u_{10}\cos(kx - \omega t)$$
$$v_1 = \frac{f}{\omega}u_{10}\sin(kx - \omega t)$$

Bottom Layer Solutions

$$u_2 = -\frac{h_1}{h_2}u_{10}\cos(kx - \omega t)$$
$$v_2 = -\frac{h_1}{h_2}\frac{f}{w}u_{10}\sin(kx - \omega t)$$

Free Surface Displacement

$$\eta_1 = 0$$
$$\eta_2 = -\frac{h_1 k}{\omega}u_{10}\cos(kx - \omega t)$$

Appendix B

Dispersion Relations

B.1 Single Layer

Single layer momentum equations are as follows :

$$\frac{du}{dt} - fv = -g\frac{d\eta}{dx} \tag{B.1}$$

$$\frac{dv}{dt} + fu = -g\frac{d\eta}{dy} \tag{B.2}$$

$$\frac{dw}{dt} + g = -g\frac{d\eta}{dz} \tag{B.3}$$

The continuity equation is as follows :

$$h(\frac{du}{dx} + \frac{dv}{dy}) + \frac{d\eta}{dt} = 0 \tag{B.4}$$

A plane wave solution of the following form will be applied to equations (B.1) - (B.4) :

$$(u, v, \eta) \sim (u_o, v_o, \eta_o) \exp i(kx - \omega t) \tag{B.5}$$

Without loss of generality we will assume the wave is solely propagating in the x direction. Applying a plane wave solution to Equations B.1 - Equation B.4 yields the following matrix equation.

$$\begin{bmatrix} -w*i & -f & g*k*i \\ f & -w*i & 0 \\ h_1*k*i & 0 & -w*i \end{bmatrix} \begin{bmatrix} u_1 \\ v_1 \\ \eta_1 \end{bmatrix} = 0$$

The determinant of the square matrix must be zero in order to not have a trivial solution.

$$det \begin{bmatrix} -w*i & -f & g*k*i \\ f & -w*i & 0 \\ h_1*k*i & 0 & -w*i \end{bmatrix} = 0$$

This implies :

$$\omega^2 = f^2 + ghk^2 \tag{B.6}$$

This is the barotropic dispersion relation. Notice that this dispersion relation implies that $\omega > f$.

B.2 Double Layer

The momentum equation for a two layer system, assuming a rigid lid approximation, are as follows :

Top Layer	**Bottom Layer**
$\frac{du_1}{dt} - fv_1 = -g\frac{d\eta_1}{dx}$	$\frac{du_2}{dt} - fv_2 = -g'\frac{d\eta_2}{dx} - g\frac{d\eta_1}{dx}$
$\frac{dv_1}{dt} + fu_1 = -g\frac{d\eta_1}{dy}$	$\frac{dv_2}{dt} + fu_2 = -g'\frac{d\eta_2}{dy} - g\frac{d\eta_1}{dy}$
$h_1\left(\frac{du_1}{dx} + \frac{dv_1}{dy}\right) + \frac{d\eta_1}{dt} - \frac{d\eta_2}{dt} = 0$	$h_2\left(\frac{du_1}{dx} + \frac{dv_1}{dy}\right) + \frac{d\eta_2}{dt} = 0$

The following plane wave solution was applied to the latter momentum equations :

$$(u, v, \eta) \sim (u_o, v_o, \eta_o) \exp i(kx - \omega t) \tag{B.7}$$

Without loss of generality the wave solution is purely in the x direction. Applying this wave solution yields the following matrix equation :

$$\begin{bmatrix} -w*i & -f & 0 & 0 & g*k*i & 0 \\ f & -w*i & 0 & 0 & 0 & 0 \\ 0 & 0 & -w*i & -f & g*k*i & gp*k*i \\ 0 & 0 & f & -w*i & 0 & 0 \\ h_1*k*i & 0 & 0 & 0 & 0 & w*i \\ 0 & 0 & h_2*k*i & 0 & 0 & -w*i \end{bmatrix} \begin{bmatrix} u_1 \\ v_1 \\ u_2 \\ v_2 \\ \eta_1 \\ \eta_2 \end{bmatrix} = 0$$

The determinant of the square matrix must be zero in order to not have a trivial solution.

$$det \begin{bmatrix} -w*i & -f & 0 & 0 & g*k*i & 0 \\ f & -w*i & 0 & 0 & 0 & 0 \\ 0 & 0 & -w*i & -f & g*k*i & gp*k*i \\ 0 & 0 & f & -w*i & 0 & 0 \\ h_1*k*i & 0 & 0 & 0 & 0 & w*i \\ 0 & 0 & h_2*k*i & 0 & 0 & -w*i \end{bmatrix} = 0$$

The zero determinant implies :

$$\omega_{BC}^2 = f^2 + g'h'k^2, \quad \text{where} \quad g' = g\frac{\Delta\rho}{\rho_o}, \quad h' = \frac{h_1 h_2}{h_1 + h_2} \tag{B.8}$$

This is the baroclinic dispersion relation. Notice that this dispersion relation implies that $\omega > f$.

Appendix C

Wave Climate

C.1 Wavelength

The solutions from the two layer system are provided below :

Top Layer Solutions

$$u_1 = u_{10}\cos(kx - \omega t)$$
$$v_1 = \frac{f}{\omega}u_{10}\sin(kx - \omega t)$$

Bottom Layer Solutions

$$u_2 = -\frac{h_1}{h_2}u_{10}\cos(kx - \omega t)$$
$$v_2 = -\frac{h_1}{h_2}\frac{f}{w}u_{10}\sin(kx - \omega t)$$

Free Surface Displacement

$$\eta_1 = 0$$
$$\eta_2 = -\frac{h_1 k}{\omega}u_{10}\cos(kx - \omega t)$$

The magnitude of the internal interface is given by :

$$|\eta_2| = \frac{h_1 k}{\omega}u_{10} \tag{C.1}$$

Solving this for k yields the following equation :

$$\frac{|\eta_2|\omega}{h_1 u_{10}} = k \tag{C.2}$$

Since $k = \frac{2\pi}{\lambda}$, the latter equation can be solved for λ.

$$\frac{|\eta_2|\omega}{h_1 u_{10}} = k \tag{C.3}$$

$$\frac{|\eta_2|\omega}{h_1 u_{10}} = \frac{2\pi}{\lambda} \tag{C.4}$$

$$\frac{2\pi h_1 u_{10}}{|\eta_2|\omega} = \lambda \tag{C.5}$$

We now have an expression for the wavelength of inertial waves. Where u_{10} is the magnitude of zonal velocity in the upper layer, ω is the frequency of the wave ($\omega \approx f$), $|\eta_2|$ is the amplitude of the internal interface, and h_1 is the depth of the top layer. amplitude of the internal interface can be estimated using the amplitude of a linear wavelet tuned to the inertial frequency. The depth of the top layer can be estimated by low pass filtering the time series of the thermocline depth.